

In-Situ Vibrational Spectroscopic Studies on Model Catalyst Surfaces at Elevated Pressures

Emrah Ozensoy · Evgeny I. Vovk

Published online: 30 July 2013

© Springer Science+Business Media New York 2013

Abstract Elucidation of complex heterogeneous catalytic mechanisms at the molecular level is a challenging task due to the complex electronic structure and the topology of catalyst surfaces. Heterogeneous catalyst surfaces are often quite dynamic and readily undergo significant alterations under working conditions. Thus, monitoring the surface chemistry of heterogeneous catalysts under industrially relevant conditions such as elevated temperatures and pressures requires dedicated in situ spectroscopy methods. Due to their photons-in, photons-out nature, vibrational spectroscopic techniques offer a very powerful and a versatile experimental tool box, allowing real-time investigation of working catalyst surfaces at elevated pressures. Infrared reflection absorption spectroscopy (IRAS or IRRAS), polarization modulation-IRAS and sum frequency generation techniques reveal valuable surface chemical information at the molecular level, particularly when they are applied to atomically well-defined planar model catalyst surfaces such as single crystals or ultrathin films. In this review article, recent state of the art applications of in situ surface vibrational spectroscopy will be presented with a particular focus on elevated pressure adsorption of

probe molecules (e.g. CO, NO, O₂, H₂, CH₃OH) on monometallic and bimetallic transition metal surfaces (e.g. Pt, Pd, Rh, Ru, Au, Co, PdZn, AuPd, CuPt, etc.). Furthermore, case studies involving elevated pressure carbon monoxide oxidation, CO hydrogenation, Fischer–Tropsch, methanol decomposition/partial oxidation and methanol steam reforming reactions on single crystal platinum group metal surfaces will be provided. These examples will be exploited in order to demonstrate the capabilities, opportunities and the existing challenges associated with the in situ vibrational spectroscopic analysis of heterogeneous catalytic reactions on model catalyst surfaces at elevated pressures.

Keywords PM-IRAS · SFG · FTIR · CO · NO · In-situ

1 Introduction

Achieving ultimate control over catalytic activity and selectivity in heterogeneous catalytic reactions demands addressing not only the sophisticated macroscopic engineering problems such as reactor design and mass/heat transfer but it also requires tackling the fundamental scientific challenges at the molecular level. Thus, a detailed understanding of the complex morphology, chemical composition and electronic structure of the heterogeneous catalytic surfaces is the key for designing new catalytic processes which are efficient, sustainable, renewable and environmentally friendly. Unfortunately, most of the conventional spectroscopic or diffraction techniques that are commonly used for routine material characterization fail to provide a truly surface-sensitive description of the catalyst surfaces at the molecular level.

This article is dedicated to late D. Wayne Goodman, my Ph.D. advisor, an outstandingly brilliant scientist, a truly inspirational character and a great scientific role model (E.O.).

E. Ozensoy (✉) · E. I. Vovk
Department of Chemistry, Bilkent University,
06800 Ankara, Turkey
e-mail: ozensoy@fen.bilkent.edu.tr

E. I. Vovk
Boreskov Institute of Catalysis, 630090 Novosibirsk,
Russian Federation

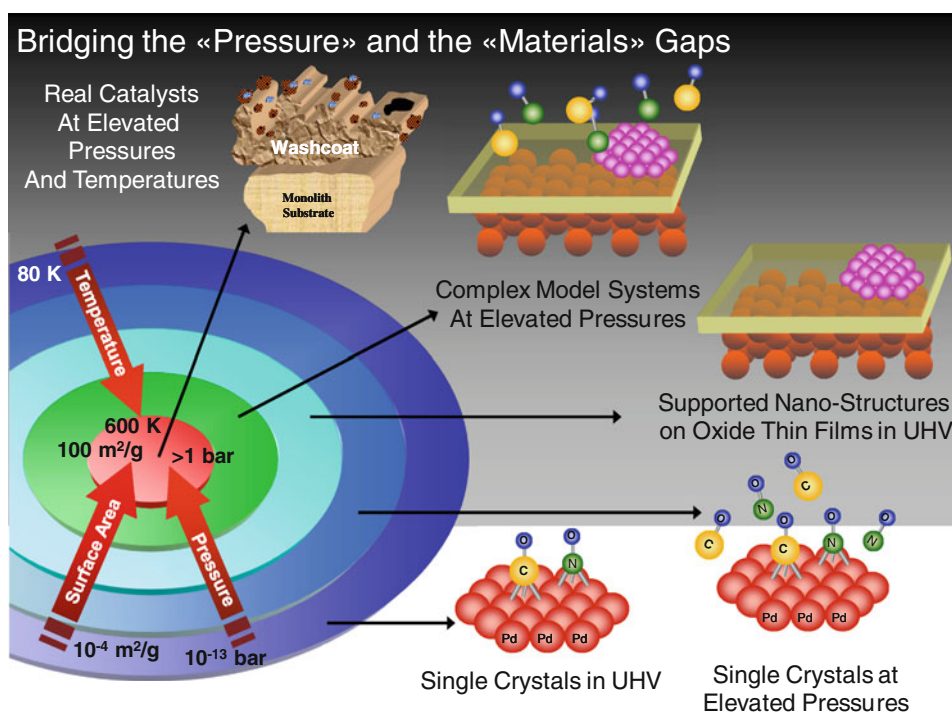
This important drawback stimulated the emergence of a multitude of novel surface-sensitive characterization techniques, such as X-ray photoelectron spectroscopy (XPS), low energy electron diffraction (LEED), scanning tunneling microscopy (STM), low energy ion scattering (LEIS), metastable impact electron spectroscopy (MIES), high resolution electron energy loss spectroscopy (HREELS) and many others [1]. However, most of these techniques rely on electrons or ions having extremely short elevated-pressure mean free paths, rendering their application to working catalysts difficult. Although some of the techniques such as XPS [2–4] and STM [5–8] evolved over time to handle elevated pressures and temperatures, majority of these surface-sensitive techniques remained to be strictly ultra-high vacuum (UHV) based approaches for model catalyst characterization, which is commonly referred as the “*pressure gap*” problem (Scheme 1) [9]. Furthermore, in situ XPS and STM techniques often fail to provide accurate or unambiguous information about the nature of the surface functional-groups which are taking part in the catalytic reaction.

On the other hand, infrared reflection absorption spectroscopy (IRAS, IRRAS or RAIRS) [10, 11], polarization modulation infrared reflection absorption spectroscopy (PM-IRAS or PM-IRRAS) [12–26] and sum frequency generation (SFG) [27–32] are essentially photon-based surface-sensitive spectroscopic techniques which are significantly less prone to the presence of a high pressure gas phase environment surrounding the catalytic surface of interest. These techniques are extremely beneficial as they

have the potential to provide a comprehensive description of the surface functional groups existing on the catalyst surface under working conditions. Thus, such surface-sensitive vibrational spectroscopic techniques provide invaluable opportunities for studying heterogeneous catalysis in real time under industrially relevant operational conditions and on complex model catalyst surfaces that can help bridge the so called “*materials gap*” (Scheme 1) [9]. Hence, in situ studies reveal new opportunities for obtaining molecular level insight about catalytic reaction mechanisms and structure–reactivity relationships.

Along these lines, in this review article, recent applications of state of the art in situ surface vibrational spectroscopic studies performed in the last decade in D. Wayne Goodman research group as well as other research groups are presented in order to demonstrate the capabilities, opportunities and the existing challenges associated with the in situ vibrational spectroscopic analysis of heterogeneous catalytic reactions on model catalyst surfaces at elevated pressures. This review is organized as follows: Sect. 2 gives a brief description of the experimental techniques relevant to the discussion. Sections 3.1.1 and 3.1.2 provide a discussion on the CO adsorption and NO adsorption, respectively which is followed by studies on CO + NO reaction (Sects. 3.2.1 and 3.2.2). Section 3.2.3 focuses on high-pressure CO + H₂ interactions which also includes studies relevant to Fischer–Tropsch chemistry. Section 3.2.4. details the mechanistic aspects of CO oxidation on platinum group metal (PGM) surfaces at elevated pressures. Section 3.2.5 deals with the catalytic methanol

Scheme 1 Bridging the “Pressure” and “Materials” gaps between surface science and catalysis



reactions on Pd and PdZn based model catalysts. Finally, an overall assessment of the reviewed work as well as a brief outlook is provided in Sect. 4.

2 Experimental

Experiments that are discussed in this review have been performed in various custom-design multi-technique UHV surface analysis chambers, which are typically equipped with elevated pressure reactors that enable the use of in situ vibrational spectroscopic techniques (in the high-pressure mode) as well as other conventional surface analysis techniques (in the UHV mode). Further experimental details regarding the experimental hardware and procedures can be found in the relevant references cited in the text. Case studies that will be discussed in this review primarily utilize three main surface vibrational spectroscopic techniques namely, IRAS, PM-IRAS and SFG [10–34]. As the main emphasis of the current text is the applications of in situ vibrational spectroscopies, detailed operational principles and the theoretical background associated with these spectroscopic techniques will not be discussed here. Instead, only brief descriptions of these

techniques will be provided. For a more comprehensive discussion about these techniques, reader is referred to the cited references in the text and references therein.

Briefly, PM-IRAS [12–16] is a versatile in situ spectroscopic technique that yields information about the surface species at solid–liquid or gas–solid interfaces by effectively removing the contribution from the background gas or liquid phase (Fig. 1). Elimination of the vibrational contribution from gas-phase species is vital for the in situ analysis of solid–gas interfaces, as these species overwhelm the smaller IR signal corresponding to the adsorbed states. The basic operational principle of the PM-IRAS technique relies on the modulation (Fig. 1b) of a linearly polarized IR beam by dividing the linearly polarized light into an s-polarized beam (i.e. parallel to the surface of the sample), and a p-polarized beam (i.e. perpendicular to the sample surface). According to the surface selection rules of IR radiation reflected from electrically conducting surfaces (Fig. 1c), [10] species adsorbed on a metal surface can only absorb p-polarized IR light, while any molecule in the isotropic gaseous or liquid phase can absorb both p- and s-polarized IR radiation. Thus, if p-polarized IR reflection signal is subtracted from the s-polarized signal and normalized by the total intensity of both p- and s-polarized IR

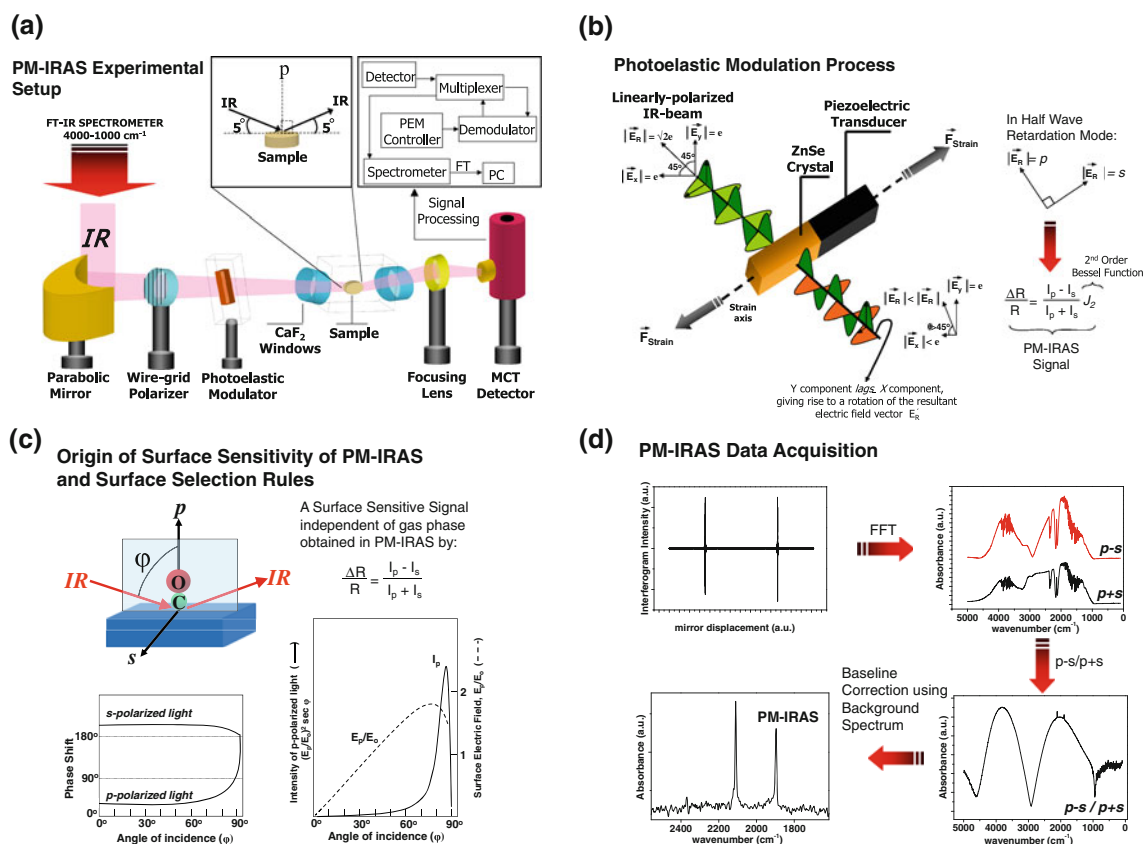


Fig. 1 Basic operational principles of PM-IRAS [17, 18]. **a** Experimental setup, **b** description of the PM process, **c** origin of PM-IRAS selection rules and surface sensitivity, **d** typical stages of the PM-IRAS data acquisition process (see text for details)

reflection beams through a virtual double-beam spectroscopic approach, a normalized surface specific IR absorption signal, practically independent of the environmental conditions, can be obtained (Fig. 1d).

On the other hand, vibrational SFG technique utilizes a second-order nonlinear optical process in which two light waves at different frequencies interact in a medium characterized by a nonlinear susceptibility tensor $\chi^{(2)}$ resulting in a wave corresponding to the sum of the frequencies of the interacting waves [28, 29, 35]. In order to obtain a SFG vibrational spectrum of adsorbates on a planar model catalyst, two picosecond laser pulses are spatially and temporally overlapped on the sample (Fig. 2) where one of the input laser pulses is in the visible frequency range having a fixed frequency (ω_{vis}), and the second laser pulse has a variable (tunable) frequency in the mid-IR region (ω_{IR}). Tuning the IR beam to the oscillatory frequency of the adsorbate results in a vibrational transition from the ground state to an excited state accompanied by a transition to a higher-energy virtual state through an anti-Stokes Raman process by the visible beam. Upon relaxation of the excited virtual state, a signal is generated with a frequency in the visible spectral region corresponding to the sum of the frequencies of the input laser beams ($\omega_{\text{SFG}} = \omega_{\text{IR}} + \omega_{\text{vis}}$). Thus, a complete vibrational spectrum can be obtained by plotting the frequency of the

input IR beam as a function of the SFG signal intensity. Selection rules associated with the SFG technique render this method a truly surface sensitive technique. In order to be SFG active, the vibrational mode of interest should be both IR and Raman active. This means SFG signal can be detected for the adsorbates at the gas/solid or liquid/solid interfaces where inversion symmetry is broken. However SFG is not allowed for the media having inversion symmetry such as bulk solids, liquids and gases [35].

3 Results and Discussion

3.1 Adsorption of Simple Probe Molecules on Model Catalyst Surfaces at Elevated Pressures

3.1.1 CO Adsorption

3.1.1.1 CO Adsorption on Pd(111) and Pd(100) Some of the early seminal vibrational spectroscopic studies on elevated-pressure CO adsorption on Pd single crystal surfaces were performed by Kuhn et al. [36] where they investigated CO/Pd(111) adsorption system within 10^{-6} –10.0 Torr via IRAS technique (Fig. 3a). A decade later, by utilizing the powerful in situ capabilities of the PM-IRAS technique,

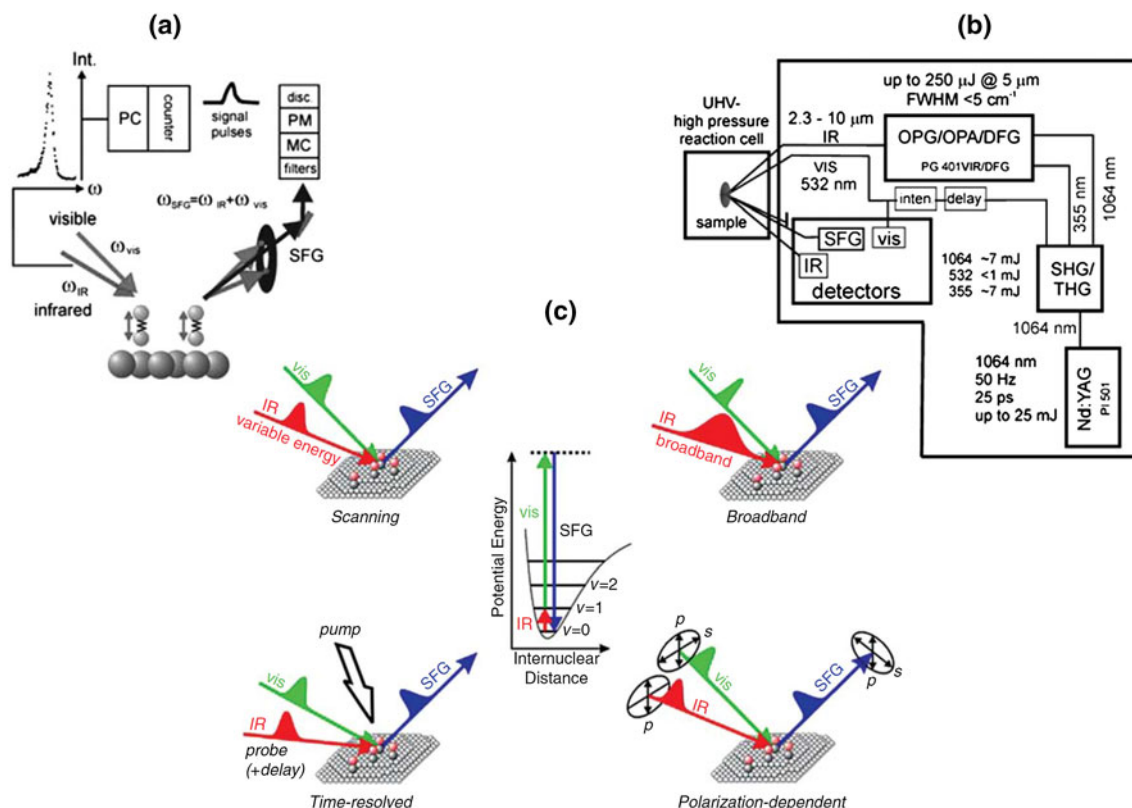


Fig. 2 Basic operational principles of SFG. **a** IR-vis SFG process [29], **b** description of an SFG spectrometer based on a Nd:YAG picosecond laser system [29], **c** various modes of operation for SFG: scanning, broadband, pump-probe and polarization-dependent operational modes [35]

similar experiments were extended to even higher CO partial pressures (i.e. $P_{\text{CO}} = 450$ Torr) by Ozensoy et al. [19] (Fig. 3b) and shortly after by Stacchiola et al. [37]. In conjunction with the high-resolution STM results on the CO/Pd(111) system [38], it has been found [19] that CO forms identical set of ordered overlayers between 10^{-6} –450.0 Torr on the clean Pd(111) substrate as a function of coverage, without any indications for the presence of adsorbate induced surface reconstructions or any unusual high-pressure phenomena. These results clearly indicated that CO/Pd(111) is a uniquely interesting adsorption system, where the nature of the coverage-dependent CO/Pd(111) overlayers are unusually invariant within nine orders of magnitude in CO pressure where similar ordered overlayers are observed at various coverages under different pressure–temperature conditions. These studies revealed that at a CO coverage of $\theta_{\text{CO}} = 0.33$ ML (ML = monolayer), a $(\sqrt{3} \times \sqrt{3})$ R 30° -1CO structure is observed (Fig. 3c) where CO resides primarily on threefold hollow sites revealing a C–O vibrational frequency of $\sim 1,850$ cm^{-1} . Upon increasing the CO coverage to $\theta_{\text{CO}} = 0.50$ ML, two coexisting $c(4 \times 2)$ -2CO phases appear in which CO is located on either the bridging sites or threefold hollow sites, yielding a vibrational signal at $\sim 1,920$ cm^{-1} . For $\theta_{\text{CO}} = 0.50$ –0.75 ML, various complex overlayer structures are formed with a CO vibrational band near $1,965$ cm^{-1} . Finally, the saturation CO coverage is obtained at $\theta_{\text{CO}} = 0.75$ ML, revealing a (2×2) -3CO structure where CO is located on both atop and threefold

hollow sites corresponding to vibrational features at 2,110 and 1,895 cm^{-1} , respectively.

These PM-IRAS experiments were also in perfect agreement with the SFG experiments performed on the CO/Pd(111) system at elevated pressures yielding results consistent with the ones discussed above [39]. It is worth mentioning that special attention has to be paid for cleaning the adsorbate gas (in this case CO) during the elevated pressure experiments (which can easily be achieved by keeping the CO container in a liquid nitrogen reservoir at 77 K throughout the experiments) in order to prevent accumulation of unwanted contaminations such as H_2O or nickel/iron carbonyls (originating from the gas tank) on the catalyst surface which can be misinterpreted as new “high-pressure” species [40]. Furthermore, SFG studies [40] on the CO adsorption on the defect-rich Pd(111) surfaces revealed the presence of bridging CO species at low coverages with a vibrational signature at 1,980–1,990 cm^{-1} which disappeared at high coverages yielding a saturation CO overlayer similar to that of the clean Pd(111) surface. Independent PM-IRAS [20] and SFG [41, 42] studies revealed that CO dissociation was not observed neither on clean nor on defect-rich Pd(111).

CO adsorption on the Pd(100) single crystal surface was also investigated by Szanyi et al. [43] within 10^{-6} –1.0 Torr via IRAS technique where the presence of only bridging CO was observed for all coverages ($0 \text{ ML} < \theta_{\text{CO}} < 0.8 \text{ ML}$) with a CO vibrational frequency ranging from 1,895 to 1,995 cm^{-1} .

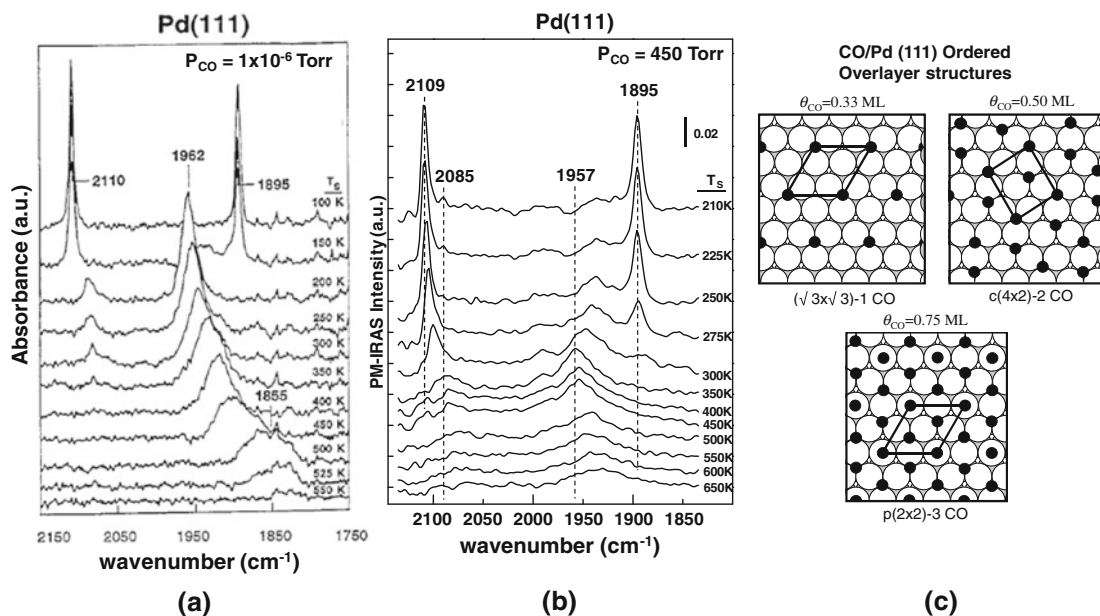


Fig. 3 **a** In-situ IRAS data for CO adsorption on Pd(111) at $P_{\text{CO}} = 1 \times 10^{-6}$ Torr [36]; **b** in situ PM-IRAS data for CO adsorption on Pd(111) at $P_{\text{CO}} = 450$ Torr [19]; **c** ordered CO

overlayer structures on the Pd(111) single crystal surface. Note that an alternative $c(4 \times 2)$ -2CO structure containing only bridging CO molecules is also possible for $\theta_{\text{CO}} = 0.50$ ML

3.1.1.2 CO adsorption on Pd Nanoparticles Deposited on Planar Metal Oxide Ultrathin Films Grown on Metal Substrates (CO/Pd/SiO₂/Mo(112) and CO/Pd/Al₂O₃/Ni(110)) Elevated pressure CO adsorption experiments on Pd single crystals were also extended to more complex model catalyst surfaces such as metal nanoparticles deposited on metal oxide ultrathin films. These structurally complex model catalyst systems enable investigation of important catalytic phenomena associated with the presence of 3D nanostructures revealing different types of surface defects (e.g. coordinatively unsaturated surface sites, point defects, edges, steps, kinks, etc.) which is crucial for efforts towards bridging the “materials gap” (Scheme 1). Such model catalyst surfaces are also suitable for studying particle size effects and structure sensitivity of catalytic reactions. There exists numerous UHV surface science studies on metal nanoparticles deposited on ultrathin films [44, 45] however, in situ investigation of such surfaces under elevated pressures has been viable only recently.

The first elevated-pressure PM-IRAS study on a metal nanoparticle system deposited on a crystalline ultrathin metal oxide film grown on a metallic substrate was performed by Ozensoy et al. [20] where they investigated CO adsorption on the Pd (~3.5 nm)/SiO₂/Mo(112) model catalyst surface at 185 mbar (Fig. 4). Comparison of the PM-IRAS data given in Fig. 4a with former UHV studies on CO/Pd(111) [36] and CO/Pd(100) [40] suggested that the silica supported Pd nanoparticles predominantly exhibited $\langle 111 \rangle$ facets with a minor contribution from $\langle 100 \rangle$ facets. Along these lines, 2,089 cm⁻¹ was attributed to CO species adsorbed on the atop sites of the $\langle 111 \rangle$ facets of the Pd nanoclusters while the shoulder features located at 2,071 and 2,045 cm⁻¹ were assigned to CO residing on defect sites of the Pd nanoparticles such as steps or edges. Furthermore, the vibrational features located at 1,957 and 1,895 cm⁻¹ in Fig. 4a are associated with the CO molecules occupying bridging and threefold hollow sites of the $\langle 111 \rangle$ facets, respectively. Annealing-cooling cycles performed in the presence of CO gas phase on these two different model catalyst surfaces suggested that although such a treatment leads to the CO dissociation and the accumulation of carbonaceous species on the silica-supported Pd nanoparticles at elevated pressures, evident by the irreversible attenuation of the IR signal intensities and the existence of C-deposit (i.e. 271 eV signal) in the Auger electron spectra (AES) obtained after thermal cycles (Fig. 4a), CO adsorption on Pd(111) is perfectly reversible even at elevated pressures without any indication of CO dissociation [20]. Furthermore, it was argued that CO molecules residing on the bridging or atop sites of the steps of the Pd nanoclusters were likely to be responsible for CO dissociation. It was proposed that after the initial dissociation of CO on the defect sites, atomic C and O diffuse to

the neighboring atop (2,089 and 2,071 cm⁻¹) and bridging sites (2,045 cm⁻¹) in close proximity of the active sites. Attenuation of the broad vibrational band at 2,089 cm⁻¹ then occurs. In a second anneal-cool cycle, further CO dissociation results in the spill-over of atomic C and O over the entire Pd cluster, resulting in nonselective attenuation of all vibrational features and to complete poisoning of the Pd clusters [20]. It is worth mentioning that CO dissociation over Pd surfaces is still a rather controversial issue where there exist studies in the literature reporting the dissolution of atomic C in the Pd(110) single crystal lattice and hence obscuring the detection of the dissociation process [46], as well as other studies on Pd/Al₂O₃ high surface area materials ruling out CO dissociation over supported Pd nanoparticles [47].

Elevated-pressure CO adsorption on supported Pd nanoparticles deposited on alumina ultrathin films grown on NiAl(110) substrate was also studied comprehensively via SFG technique [39, 40, 48–50]. For instance, influence of the particle size on the nature of the Pd adsorption sites existing on the supported Pd nanoparticles were demonstrated (Fig. 5) [48] where it was shown that the CO molecules prefer to adsorb predominantly on the atop sites on the smaller (3.5 nm) and defective/rough Pd particles for low CO coverages (Fig. 5a), while on the bigger (6 nm) Pd particles exhibiting larger planar facets, CO is also found to adsorb on bridging sites (Fig. 5b). Upon increasing the surface CO coverage with increasing CO pressure, both atop and bridging sites are populated on both surfaces although relative population of atop sites are still higher for smaller Pd particles. It is worth mentioning that these results are in good agreement with former UHV studies performed on similar systems [21].

3.1.1.3 CO/Pt(111) CO adsorption on Pt(111) is one of the most extensively studied surface science systems in the literature which has been investigated via a large variety of surface science tools. At a CO coverage of 0.5 ML, an ordered $c(4 \times 2)$ -2CO overlayer is formed where CO was found to adsorb on both atop and bridging sites (Fig. 6) [51–54]. For higher CO surface coverages two different compressed CO overlayers have been reported, namely the commensurate $(7 \times \sqrt{3})\text{rect}$ -10CO at $\theta_{\text{CO}} = 0.71$ ML [55] and the hexagonal Moiré structures $(\sqrt{19} \times \sqrt{19})\text{R}23.4$ -13CO at $\theta_{\text{CO}} = 0.68$ (Fig. 6) [55].

Earlier experiments performed on the CO/Pt(111) adsorption system at elevated pressures have been reviewed by Rupprechter [29]. More recently, Carrasco et al. [53] combined a detailed set of PM-IRAS and SFG experiments on this system within 10⁻⁷–100 mbar (Fig. 7) and provided a comprehensive description of the ordered high coverage (compressed) CO overlayers formed on Pt(111). PM-IRAS results in this work (Fig. 7a) revealed

Fig. 4 In-situ PM-IRAS data for elevated-pressure CO adsorption on **a** Pd (~3.5 nm)/SiO₂/Mo(112) and **b** Pd(111) model catalyst surfaces. *Top* spectra in each *panel* show the initial CO adsorption on the clean model catalyst surfaces while the remaining spectra were obtained after annealing-cooling cycles in the presence of the CO gas phase. *Inset* in (a) shows the C accumulation in AES after multiple annealing-cooling cycles due to the CO dissociation on the silica supported Pd particles, while CO dissociation was not observed on Pd(111) upon a similar treatment [20]

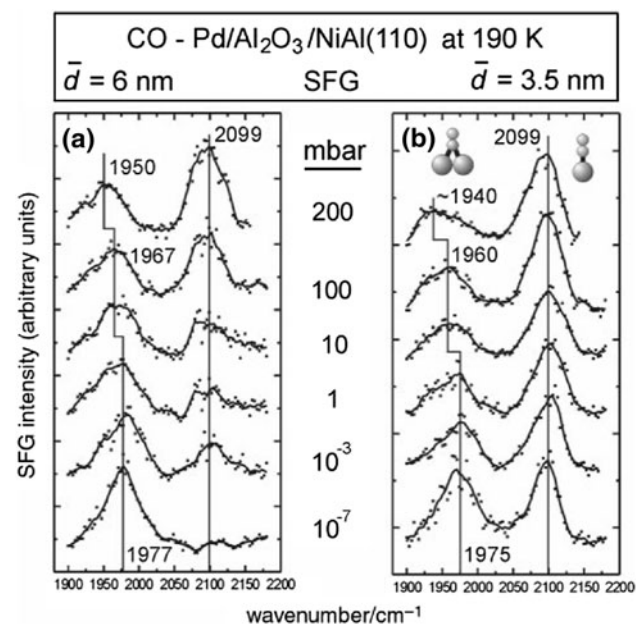
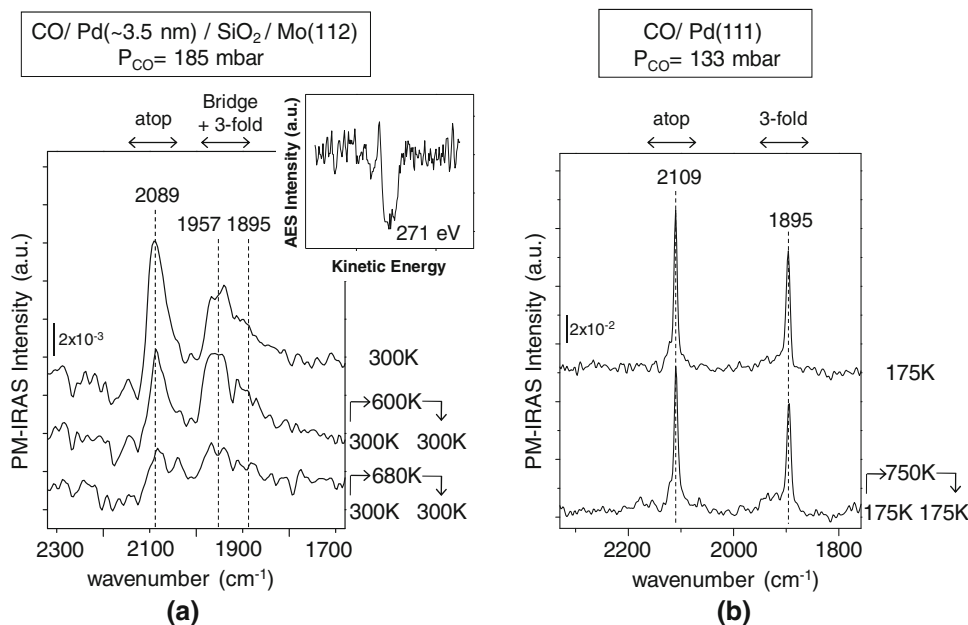


Fig. 5 CO adsorption on alumina supported Pd nanoparticles via SFG [48]. **a** Relatively ordered Pd nanoparticles with an average diameter of 6 nm grown at 300 K and **b** defective 3.5 nm Pd particles grown at 90 K. Population of a *top* sites is higher for defective/rough Pd particles particularly at low CO surface coverages

the presence of two bridging CO features at 1,853 and 1,882 cm⁻¹ as well as two different atop CO features at 2,098 and 2,109 cm⁻¹. It was demonstrated in this work that the presence of two different atop CO features are due to the coexistence of two different compressed CO overlayer domains [53]. 2,100 cm⁻¹ signal was attributed to a $c(7 \times \sqrt{3})\text{rect}$ or a $c(5 \times \sqrt{3})\text{rect}$ domain which exists under kinetically hindered conditions below 200 K. On the

other hand, 2,110 cm⁻¹ signal was associated to a Moiré structure (Fig. 6c) which is formed within 200–300 K. The same study also showed that similar vibrational signatures can also be reproduced via SFG technique (Fig. 7b, c) where two atop features could be observed at 250 K while a single atop feature was detected at 300 K. These results, combined with previous results in the literature, [29] suggested that although there is no obvious pressure gap for the CO/Pt(111) adsorption system, existence of different ordered and compressed CO overlayers strictly depends on the preparation conditions of the CO overlayer and the subsequent dosing parameters such as temperature and pressure.

3.1.1.4 CO/CuPt(111) In a recent study, Andersson and Chorkendorff [56] investigated elevated-pressure CO adsorption on a CuPt surface alloy (SA) prepared on a Pt(111) substrate via PM-IRAS (Fig. 8). This study demonstrated that CO adsorption can be used to monitor the state of the CuPt(SA) under oxidizing or reducing conditions at elevated pressures. Figure 8 shows that CO adsorbs in only atop configuration on the CuPt (SA) in UHV, while exposure to 200 mbar O₂ decreases the surface coverage of CO due to CO oxidation/CO₂ formation as well as oxidation of the CuPt (SA). It was shown that this oxidized CuPt (SA) could be reduced to its original state by 100 mbar CO adsorption and subsequent evacuation to UHV. This study also demonstrated that elevated pressure CO reduction is a successful method to regenerate CuPt (SA) surfaces which are initially treated with CO + H₂ (P_{tot} = 220 mbar, 4 % CO) within 300–573 K or CO + H₂O (P_{tot} = 17 mbar, 50 % CO) demonstrating the stability of this surface as a potentially versatile model catalyst system.

Fig. 6 Ordered CO overlayers on Pt(111) at high coverages [53]: **a** $c(4 \times 2)$ or $(2 \times \sqrt{3})\text{rect}$ at $\theta_{\text{CO}} = 0.5$, **b** $c(7 \times \sqrt{3})\text{rect}$ ($\theta_{\text{CO}} = 0.71$), **c** $(\sqrt{19} \times \sqrt{19})\text{R}23.4$ -13CO ($\theta_{\text{CO}} = 0.68$)

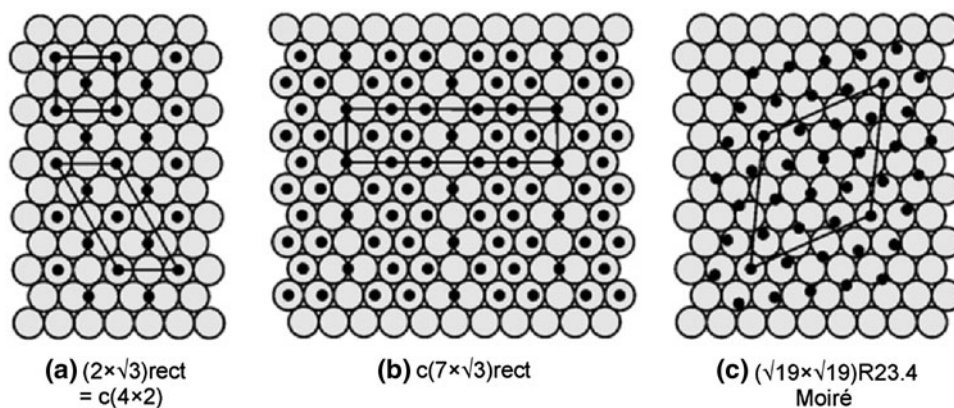
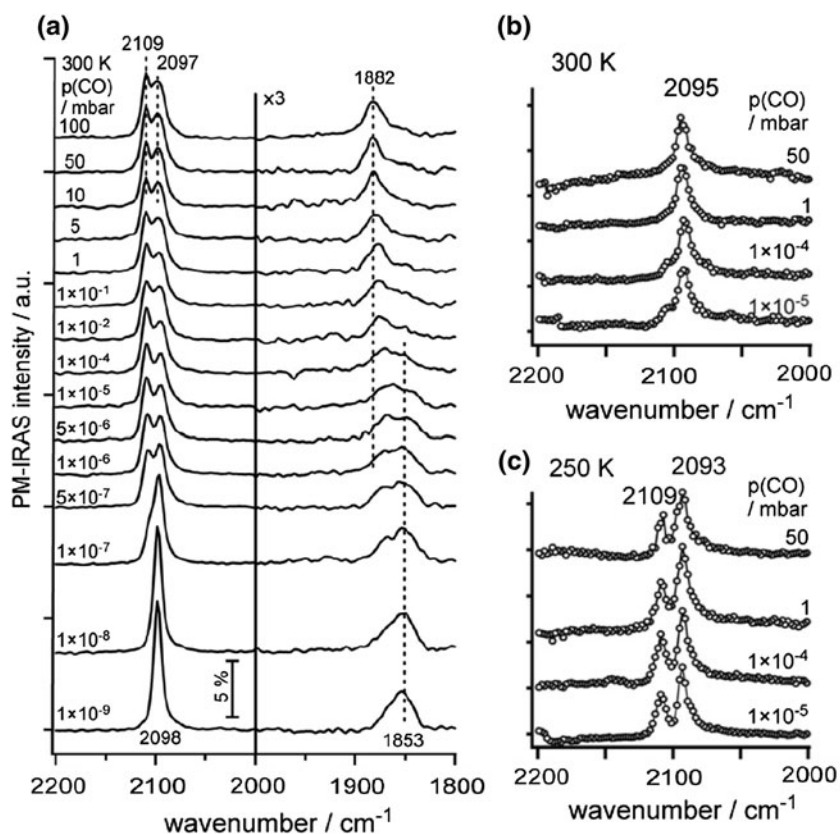


Fig. 7 CO adsorption on Pt(111) via **a** PM-IRAS within 10^{-9} mbar $< P_{\text{CO}} < 100$ mbar at 300 K and via SFG within 10^{-5} mbar $< P_{\text{CO}} < 100$ mbar at **b** 300 K and **c** 250 K [53]

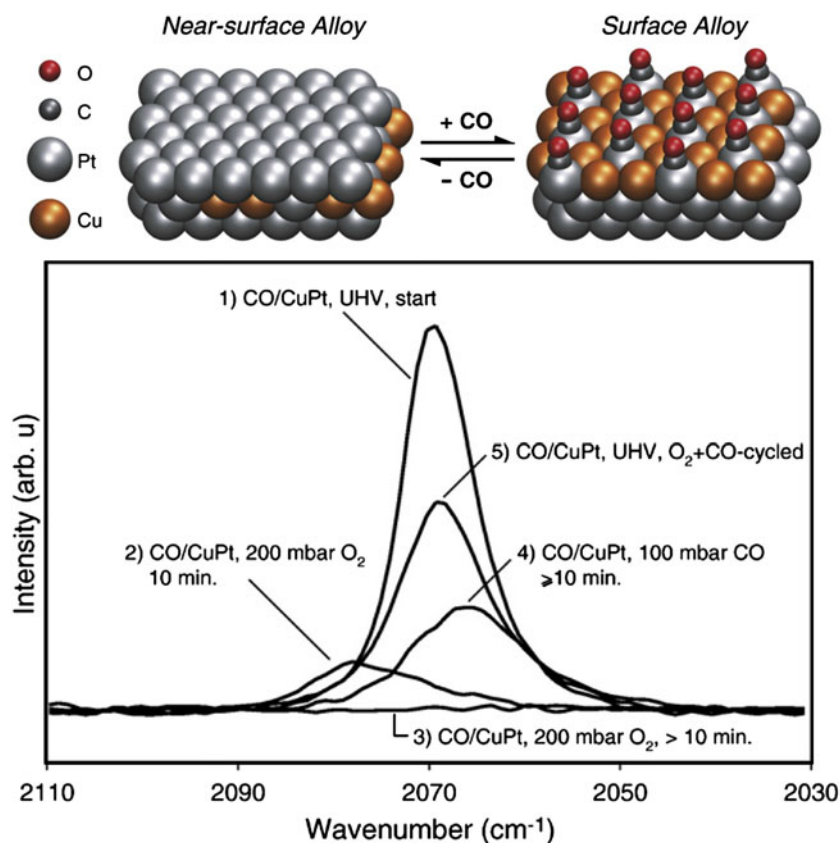


3.1.1.5 CO/Au(111), CO/Au(100) and CO/Au/TiO_x/Pt(111) Although gold has been historically considered as a poorly active element in catalytic reactions, in their ground breaking study in 1989, Haruta et al. [57, 58] showed that Au can indeed be an extremely active metal in various catalytic reactions, especially when prepared in the form of supported nanoparticles. Later, Goodman and co-workers [59] demonstrated the quantum size effect for Au nanoparticles supported on TiO₂, unraveling the complex alterations occurring in the electronic structure of Au nanoparticles as a function of particle size which had a direct impact on the catalytic activities of these systems. Owing to these pioneering studies as well as other similar

studies, today there exists a large family of homogeneous and heterogeneous catalytic reactions which utilize Au as an active catalytic component [60]. Along these lines, investigation of Au model catalyst surfaces at elevated pressures via in situ vibrational spectroscopies [61–71] is of particular interest, since such studies provide invaluable fundamental information regarding the surface structure and the nature of the adsorption sites of the challengingly complex industrial Au-based catalysts.

Nakamura et al. [62] and Piccolo and co-workers [71] investigated CO adsorption on Au single crystal model catalyst surfaces at elevated pressures via PM-IRAS technique (Fig. 9). They observed that at $T > 273$ K, CO

Fig. 8 CO adsorption on CuPt surface alloy (SA) on Pt(111) at room temperature via PM-IRAS [56]. Spectrum (1) corresponds to CO adsorption on CuPt(SA) in UHV. Spectra (2–3) show the CO adsorbed on CuPt(SA) in UHV which is subsequently oxidized in 200 mbar O₂. Spectrum (4) corresponds to the subsequent reduction of surface (3) in 100 mbar CO. Spectrum (5) corresponds to the evacuation of surface (4) to UHV conditions



vibrational signal was below the detection limit for CO pressures less than 10^{-2} Torr. For CO pressures above 10^{-2} Torr, CO was found to adsorb in atop configuration on Au(100), Au(111), Au(311) [62] and Au(110) [71]. Nakamura et al. [62] also reported that while atop CO species adsorbed on the terraces of Au(100), Au(111), Au(311) surfaces yielded a typical vibrational signature within 2,070–2,080 cm^{-1} , CO adsorbed on step edges in an atop fashion revealed a higher vibrational frequency at 2,117 cm^{-1} . This argument is in line with the work of Piccolo and co-workers [71] who observed an adsorbate (i.e. CO) induced reconstruction of the Au(110) surface via STM along with a CO vibrational signal at 2,110 cm^{-1} in PM-IRAS (Fig. 9d). Same authors also reported CO-induced roughening of the Au(111) surface at elevated pressures [61].

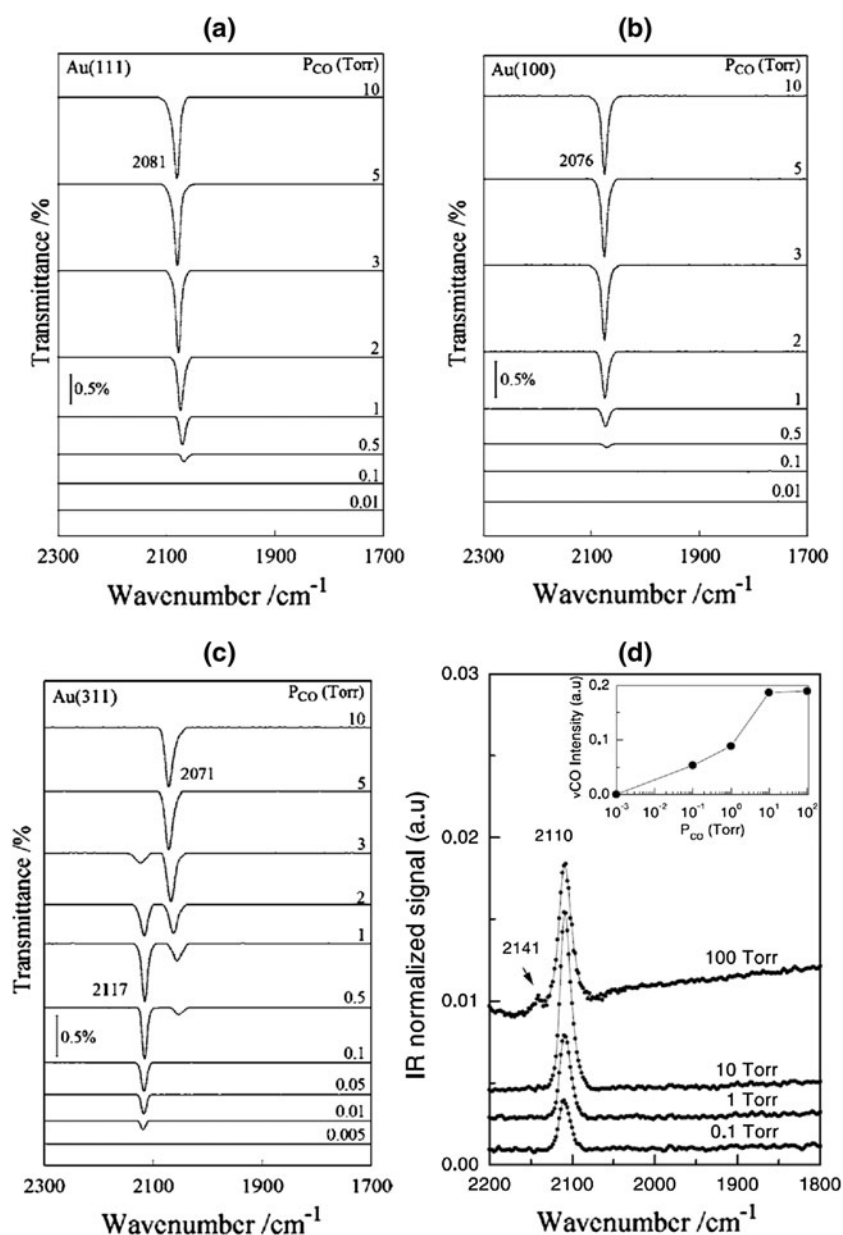
In-situ vibrational spectroscopic studies at elevated pressures were also extended to 3D Au nanoparticles with various diameters deposited on a TiO₂ ultrathin film grown on a Ru(0001) substrate by Diemant et al. [66] (Fig. 10). These results showed that on these defective and relatively small 3D Au clusters, CO vibrational frequency appeared around 2,110 cm^{-1} , consistent with the previous studies on Au single crystals suggesting that CO adsorbs in an atop fashion on Au clusters. Furthermore, CO adsorption energy values obtained from the PM-IRAS data suggested that the

adsorption energy of CO decreases from 74 to 62 kJ/mol as the average diameter of Au clusters increase from 2 nm to 4 nm. In contrast, CO adsorption energies derived from CO + O₂ mixtures in a similar fashion revealed a value of 63 kJ/mol which was independent of the Au particles size. Invariance in the CO adsorption energy as a function of Au particles size in the presence of CO + O₂ mixture was attributed to the interactions between adsorbed CO and oxygen as well as site blocking rather than any alterations in the electronic structure or morphology changes of Au particles [66]. Similar elevated-pressure CO adsorption experiments performed on Au/TiO_x/Pt(111) model catalyst surface containing reduced TiO_x nano-patches suggested that the CO chemisorption strength primarily depended on the Au nanoparticle size and morphology, where smaller Au particles revealed a higher affinity towards CO, while the Ti oxidation state and the extent of reduction in the TiO_x layer did not play a significant role [63].

3.1.2 NO Adsorption

3.1.2.1 NO/Pd(111) NO adsorption on Pd(111) has been thoroughly studied via various vibrational spectroscopic techniques under UHV conditions [21]. These studies suggested that NO forms various coverage-dependent ordered overlayers on Pd(111) with typical NO vibrational

Fig. 9 CO adsorption on various Au single crystal surfaces at elevated pressures via PM-IRAS. **a–c** Au(111), Au(100) and Au(311) at 273 K, respectively [62] and **d** Au(110) at 300 K [71]



frequencies associated with various adsorption sites that are summarized in Fig. 11. NO adsorption experiments performed on Pd(111) at moderately high NO pressures such as 13.3 mbar (Fig. 12b) [22, 23] revealed that coverage-dependent NO overlayers formed under moderately high pressures are in good agreement with similar studies performed under UHV (Fig. 12a) [23, 72].

Although NO adsorption on Pd(111) within 10^{-6} –13.3 mbar seems to suggest that no high-pressure species are formed in this adsorption system, recent PM-IRAS results and complementary theoretical calculations performed by Ozensoy et al. [22, 23] (Figs. 12c, 13) [22] showed that under extremely high NO pressures (e.g. 400 mbar) a new high-pressure (compressed) ordered

monomeric NO overlayer (i.e. (3×3) -7NO) is formed revealing a higher NO surface coverage ($\theta_{\text{NO}} = 0.778$ ML) than the conventional UHV saturation coverage of NO ($(p(2 \times 2)$ -3NO, $\theta_{\text{NO}} = 0.75$ ML). The most prominent characteristic feature of this new high-pressure NO overlayer was the increased population of threefold hollow sites of the Pd(111) surface. It is worth mentioning that $((3 \times 3)$ -7NO structure is only observed under elevated temperature–pressure conditions (300 K, $P_{\text{NO}} = 400$ mbar) and it cannot be obtained by increasing the NO surface coverage in UHV even at extremely low temperatures (e.g. 25 K) [23]. The lack of such a high coverage monomeric NO adsorption state at 25 K under UHV conditions suggests that formation of such a state requires a high

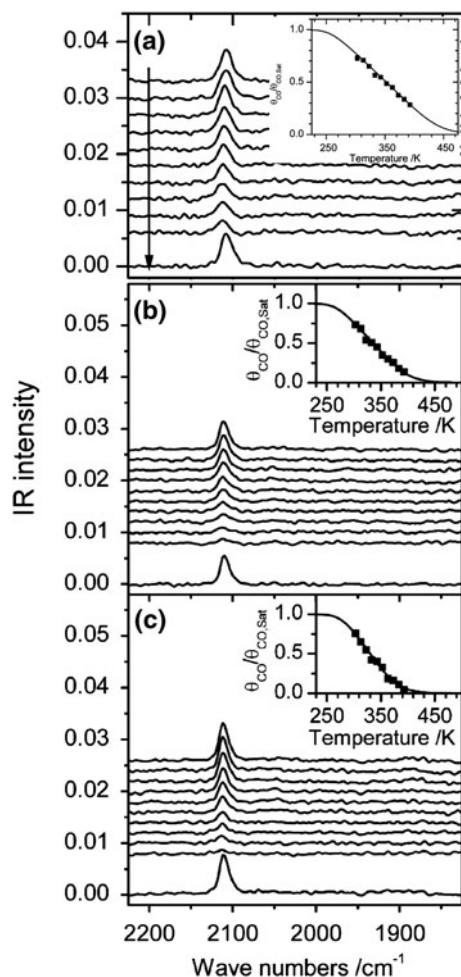


Fig. 10 PM-IRAS data for 10 mbar CO adsorption within 303–393 K on Au nanoparticles of varying sizes deposited on TiO₂/Ru(0001) [66]. In each panel, the topmost spectrum was obtained at 303 K and the temperature is increased with 10 K increments for each of the lower spectrum where the last (bottommost) spectrum was also obtained at 303 K. Insets show the variation of the normalized CO surface coverage as a function of temperature. **a** 0.21 ML Au deposit (two atomic layers thick, ~2 nm diameter particles), **b** 0.9 ML Au deposit (4–5 atomic layers thick, ~3 nm diameter particles), **c** 1.6 ML Au deposit (6 atomic layers thick, ~4 nm diameter particles)

activation barrier which can be overcome only under elevated temperature and pressure conditions. These results particularly demonstrate that simple extrapolations based on UHV experiments at low temperatures and pressures may be misleading (at least for certain cases) for describing the elevated-pressure/temperature systems as these descriptions are only accurate as long as the thermodynamic equilibrium states are also kinetically accessible.

It has been reported in the literature that in addition to the monomeric adsorption states, NO can also form dimers on Pd(111) under UHV conditions at low temperatures, where NO surface coverage exceeds the monomeric saturation coverage and forms condensed multilayers [21]. However dimeric states of NO had never been reported to

exist on Pd(111) at elevated temperatures and pressures until very recently, although such species are commonly observed on realistic high surface area catalysts under such conditions. Hess et al. [23] showed that by investigating NO adsorption via in situ PM-IRAS at high pressures (e.g. 400 mbar), existence of NO dimers (Pd-(ONNO)) and dinitrosyls (ON-Pd-NO) on Pd(111) single crystal model catalysts can be demonstrated (Fig. 14). Figure 14a illustrates the influence of the initial adsorption temperature on the nature of the high-coverage NO adsorption states formed on Pd(111) at 400 mbar NO pressure. Topmost spectrum in Fig. 14a corresponds to an initial adsorption temperature of 300 K where NO dissociation is hindered by the relatively low surface temperature. Under these conditions, a set of vibrational features located at 1855, 1826, 1779 and 1537 cm⁻¹ were observed, where 1779, 1855 and 1537 cm⁻¹ can be attributed to the NO dimer species and the 1826 cm⁻¹ can be assigned to the symmetric N = O stretch of dinitrosyl species, i.e., a species where two NO molecules are bound to the same metal center.

On the other hand, when the initial NO adsorption is performed at 650 K (middle spectrum in Fig. 14a), due to NO dissociation and partial blocking of the Pd(111) adsorption sites by dissociation products (i.e. atomic N and O) only a monomeric (3 × 3)-7NO overlayer (θ_{NO} = 0.778 ML) structure was obtained on Pd(111). Further NO dissociation induced by annealing this surface in the presence of 400 mbar NO pressure at 600 K and cooling back to 300 K (bottommost spectrum in Fig. 14a) results in the formation of the conventional monomeric UHV saturation coverage structure (i.e. p(2 × 2)-3NO, θ_{NO} = 0.75 ML). It is worth mentioning that indirect evidence for the NO dissociation on Rh(111) at 1 Torr and 300 K was also reported by Wallace et al. [73] where they have only observed atop NO adsorption on Rh(111) without threefold NO adsorption (possibly due to the occupation of the threefold sites by the NO dissociation products), although former UHV studies on this surface indicated the existence of threefold NO at high surface coverages. It is also important to point out that although dimer species can be obtained on Pd(111) under UHV conditions at 25 K by increasing NO exposure (Fig. 14 b), dinitrosyl species or the (3 × 3)-7NO monomeric compressed overlayer structure was not accessible in UHV.

3.2 Co-adsorption and Reaction on Model Catalyst Surfaces at Elevated Pressures

3.2.1 CO + NO Co-adsorption and Reaction on Pd(111)

It was illustrated in the previous sections that Pd(111) yields itself as an interesting model catalyst system where

Fig. 11 Coverage-dependent ordered monomeric NO overlayers on Pd(111) under UHV conditions

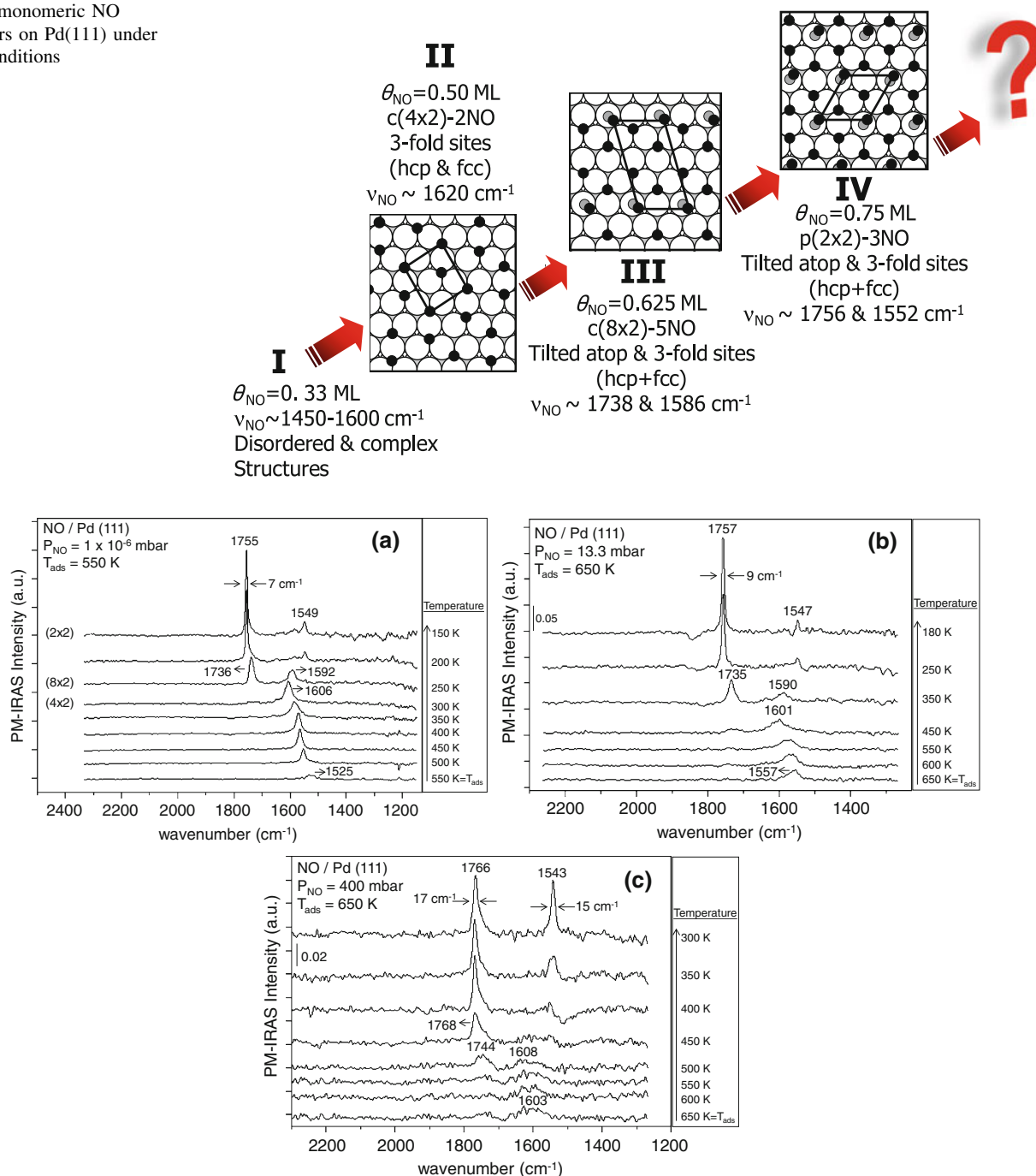


Fig. 12 NO adsorption on Pd(111) under **a** UHV (10^{-6} mbar), **b** moderately high NO pressure (13.3 mbar) and **c** elevated NO pressure (400 mbar) [22, 23]

this surface reveals almost identical behavior in UHV and at elevated pressures when used with a particular probe molecule such as CO. In contrast, another simple diatomic probe molecule such as NO, leads to interesting and novel high-pressure states such as dinitrosyls or a compressed $(3 \times 3)\text{-}7\text{NO}$ monomeric overlayer structure which are only accessible upon kinetic activation at elevated

temperatures and pressures. In a similar fashion, CO + NO reaction on Pd(111) model catalyst surface has also proven to be interesting in terms of yielding new high-pressure species that cannot be observed under conventional UHV conditions. Former UHV surface science studies on the Pd(111), Pd(100) and more advanced model catalysts prepared by depositing Pd nanoclusters on metal oxide

Calculated mean chemisorption energies, surface free energies per unit area, bond distances and bond angles for p(2×2)-3NO vs. (3×3)-7NO overlayers on Pd (111)

	p(2×2)-3NO	(3×3)-7NO
θ_{NO} (ML)	0.75	0.778
$\langle E_{\text{ads}} \rangle$ (eV/NO molecule)	-1.76	-1.67
γ (meV/Å ²)	-189	-196
$d_{\text{N-O}}$ (Å) – atop site	1.17	1.17
$d_{\text{N-O}}$ (Å) – fcc site	1.21	1.20
$d_{\text{N-O}}$ (Å) – hcp site	1.20	1.20
$d_{\text{Pd-N}}$ (Å) – atop site	1.94	1.94
$d_{\text{Pd-N}}$ (Å) – fcc site	2.08	2.07-2.11
$d_{\text{Pd-N}}$ (Å) – hcp site	2.08-2.10	2.07-2.16
$\alpha_{\text{Pd-N-O}}$ (°) – atop site	129	131

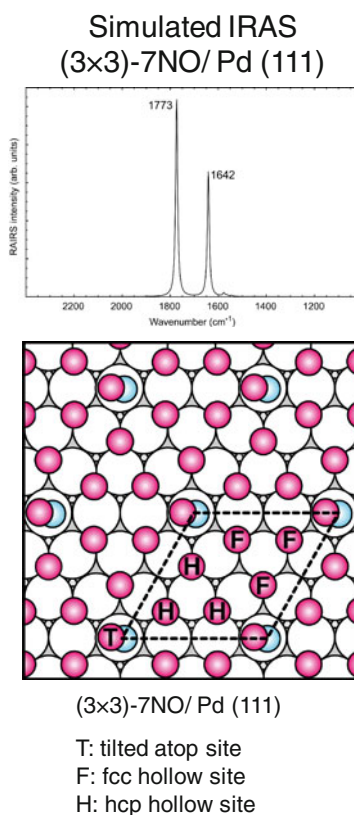


Fig. 13 Comparison of the structural parameters of the conventional UHV saturation coverage NO overlayer on Pd(111) (i.e. p(2 × 2)–3NO, $\theta_{\text{NO}} = 0.75$ ML) and the high-pressure saturation coverage state (i.e. (3 × 3)–7NO, $\theta_{\text{NO}} = 0.778$ ML). Strong 1,642 cm⁻¹ signal

ultrathin films grown on metallic substrates were reviewed in detail in recent reports and thus will not be elaborated here [18, 21].

The first in situ spectroscopic elevated pressure study for the CO + NO reaction on Pd(111) planar model catalyst surface was performed by Ozensoy et al. [18, 24–26] where they exploited in situ PM-IRAS technique to investigate CO + NO reaction at 240 mbar (Fig. 15). In these studies, it was shown that in addition to the conventional monomeric CO and NO species that are adsorbed on various adsorption sites of the hexagonal Pd(111) surface (such as atop, bridging, threefold), presence of other surface reaction intermediates such as isocyanate (–NCO) and isocyanic acid (HNCO) were also detected on Pd(111) at elevated temperatures and pressures where the source of H was suggested to be the bulk of the Pd crystal. Although –NCO and HNCO species have been detected [74] on numerous industrial supported precious metal catalysts during the CO + NO reaction and in the presence of H₂ or H₂O; such species have been elusive to detect in former UHV surface science studies. Thus, the in situ PM-IRAS experiments performed with $P_{\text{CO+NO}} = 10^{-6}$, 10^{-4} , 10^{-2} and 10^{-1} mbar at 600 K (Fig. 15a) demonstrated that

in the computationally simulated IRAS spectrum based on the (3 × 3)–7NO overlayer structure depicted in the figure is consistent with the increase in the population of the threefold sites in the experimental PM-IRAS results [22]

detection of –NCO and HNCO species requires a kinetic activation which can only be fulfilled at sufficiently high temperatures and pressures. It is worth emphasizing that there exists also additional controversial work in the literature regarding the existence of HNCO species on Pd single crystal surfaces [75, 76].

3.2.2 CO + NO Co-adsorption and Reaction on AuPd(100)

Elevated pressure CO + NO reaction has also been recently investigated on more advanced bimetallic AuPd(100) model catalyst surfaces via in situ PM-IRAS technique (Fig. 16) [69]. These studies indicated that the alloy catalyst exhibited higher CO₂ formation rates below 550 K than Pd single crystals due to the lower adsorption energy of NO and CO on the AuPd(100) surface leading to the presence of a larger number of available unoccupied surface sites for NO dissociation at lower temperatures. Furthermore, unlike Pd single crystal surfaces, adsorption energy of NO was found to be lower than that of CO for the CO:NO = 1:1 mixture. Also, CO + NO reaction on the AuPd(100) alloy surface revealed significantly different

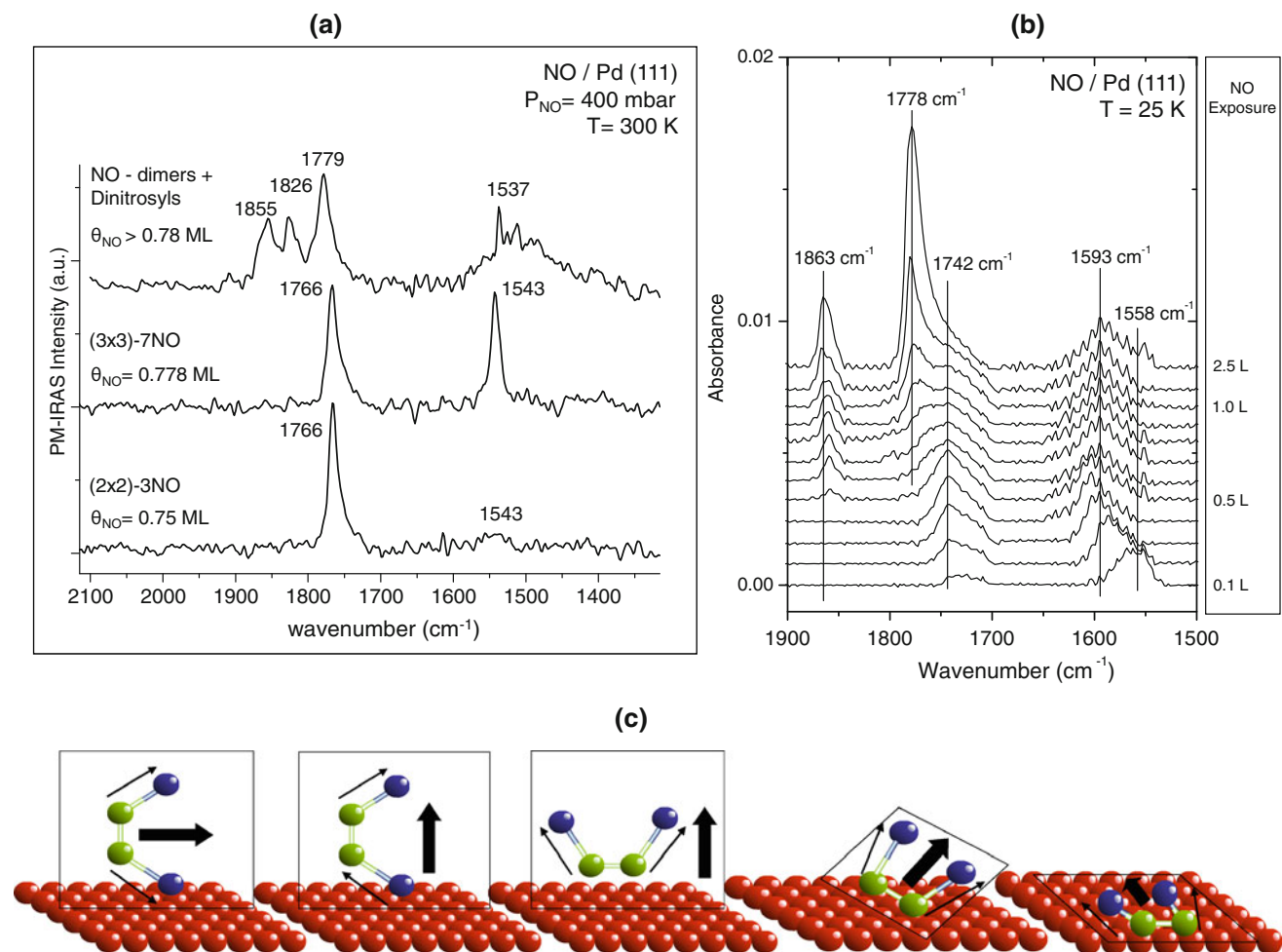


Fig. 14 a In situ PM-IRAS data for NO adsorption on Pd(111) at $P_{\text{NO}} = 400 \text{ mbar}$ and $T = 300 \text{ K}$ after various pretreatments: (*top*) initial adsorption at 300 K; (*middle*) initial adsorption at 650 K and subsequent cooling to 300 K; (*bottom*) initial adsorption at 650 K, cooling back to 300 K, second annealing at 600 K, cooling back to

300 K. **b** Coverage-dependent NO adsorption on Pd(111) in UHV at 25 K indicating the formation dimers (but no dinitrosyls). **c** Some of the possible adsorption configurations of NO dimers on Pd(111) [23]

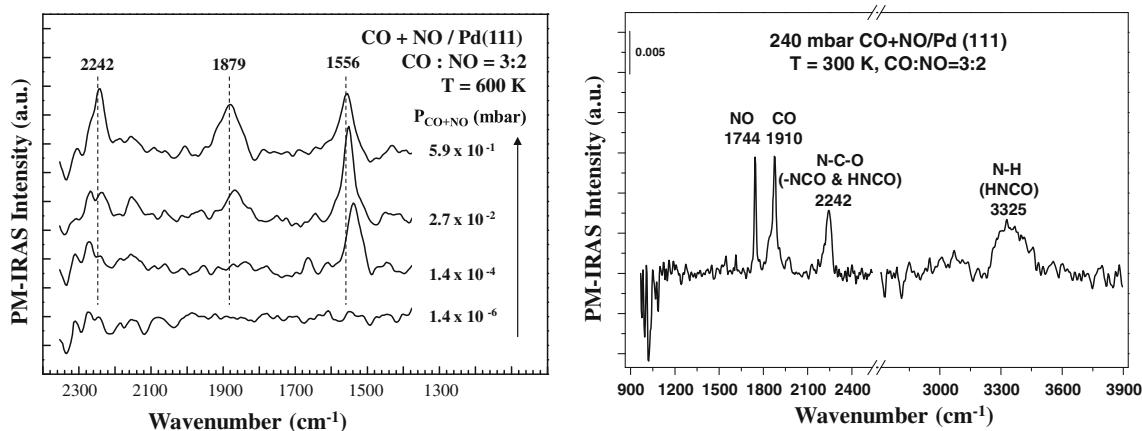
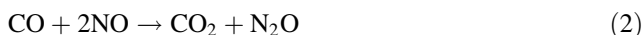


Fig. 15 a In-situ PM-IRAS data for CO + NO reaction on Pd(111) at 600 K and at various pressures showing the pressure barrier for the detection of $-\text{NCO}/\text{HNCO}$ species [24]. **b** Observation of $-\text{NCO}$ and

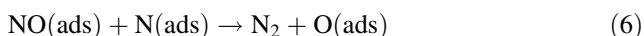
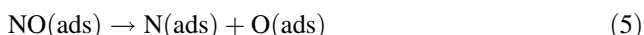
HNCO species during CO + NO reaction on Pd(111) at 240 mbar. Spectrum was obtained by dosing the gas mixture at 600 K and subsequently cooling to 300 K [26]

CO and NO reaction orders and a much higher selectivity towards N_2 , suggesting that Au promotion in conventional three way catalysts (TWC) may assist solving the “cold start” problem.

Two global reaction pathways were proposed for this system [69]:



With the following elementary reaction steps:



It was demonstrated in this study that the global reaction pathway (1) dominates the AuPd(100) catalyst. Relatively small NO vibrational signals in Fig. 16a and b, supports the decreased adsorption strength of NO with respect to CO on the AuPd(100) model catalyst surface at various temperatures, total pressure and relative gas compositions. Two different kinetic regimes were apparent for the CO + NO reaction the AuPd(100) surface (Fig. 16c): a lower activation energy regime below 500 K corresponding to an apparent activation energy of 23 kJ/mol and a higher activation energy regime above 500 K with an apparent activation energy of 40 kJ/mol. Figure 16d also clearly

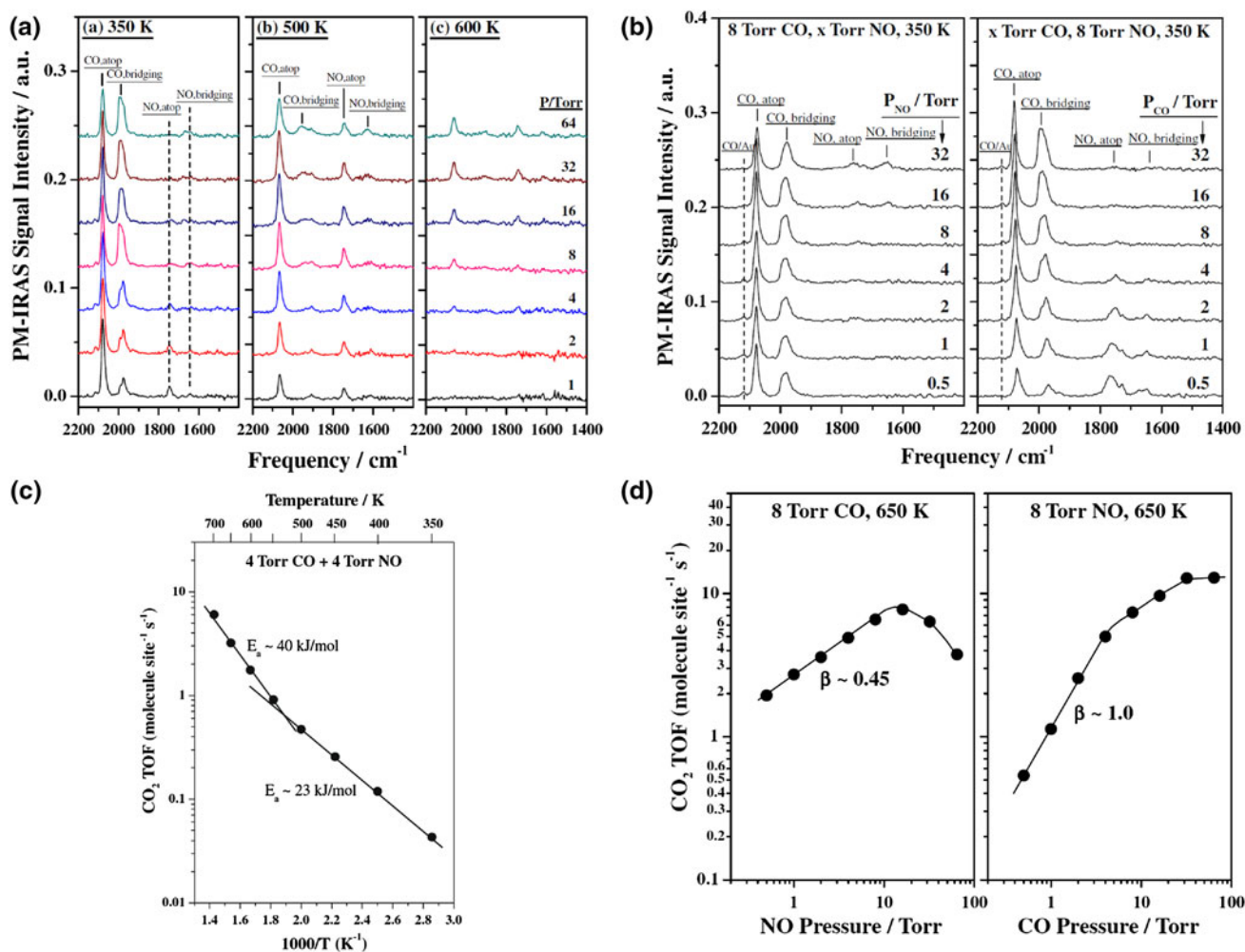


Fig. 16 **a** In-situ PM-IRAS data for CO + NO reaction on AuPd(100) surface at 350, 500 and 600 K under $P_{\text{CO}+\text{NO}} = 1\text{--}64$ Torr where CO:NO ratio is equal to 1. **b** In-situ PM-IRAS data for CO + NO reaction on AuPd(100) at 350 for various CO:NO

relative compositions. **c** Arrhenius plot for CO + NO reaction on AuPd(100) (4 Torr CO + 4 Torr NO). **d** CO₂ conversion as function of varying NO and CO partial pressures at 650 K [69]

indicates that at low CO and NO pressures, positive orders of reaction rates were detected for both CO and NO, indicating that due to the low adsorption energy of CO and NO on the AuPd(100) surface, none of these reactants act as inhibitors or surface site blockers. On the other hand for NO-rich compositions reaction rate was found to be decreasing with increasing NO partial pressure, revealing the negative effect of site blocking upon the accumulation of atomic N and atomic O (i.e. NO dissociation products) on the surface.

The same study [69] also investigated the CO + O₂ + NO reaction on the AuPd(100) bimetallic alloy surface at elevated pressures, where it was reported that low-pressure NO promotes CO + O₂ reaction via the formation of gas phase NO₂, providing a more efficient atomic oxygen supplier than O₂ below 600 K. However above a critical NO pressure, NO₂ leads to the surface oxidation, inhibiting CO₂ formation. Furthermore, it was also demonstrated that Pd/Au surface atom ratio on the AuPd(100) alloy undergoes variations as a function of the composition and the total pressure of the reactant mixture and these subtle, yet important changes can be effectively followed by the powerful PM-IRAS technique.

3.2.3 CO + H₂ Co-adsorption and Reaction

3.2.3.1 CO + H₂ Co-adsorption and Reaction on Co(0001) CO + H₂ co-adsorption and reaction is particularly important for Fisher–Tropsch (FT) reaction where cobalt based supported catalysts are actively used in the industry. Thus, CO + H₂ system was studied at elevated pressures on Co(0001) model catalyst surfaces by Shell research laboratories [77]. It was shown that the clean/low-defect density Co(0001) surface functions as a methanation catalyst with a low chain growth probability (α) factor, rather than a true FT catalyst [77–79]. On the other hand, polycrystalline Co foils exhibiting a high surface defect density was found to be more efficient FT catalysts with a higher α factor. Thus, Oosterbeek exploited PM-IRAS technique in order to investigate CO adsorption on clean Co(0001) surface and determined the CO adsorption configurations (Fig. 17a). At low pressures, CO preferred atop sites while increasing pressure led to threefold and bridging adsorption configurations. CO adsorption on an annealed (low-defect density) Co(0001) surface was also compared with that of a defective Co(0001) model catalyst surface which was prepared via extensive ion bombardment (Fig. 17b). It was shown that the presence of defects led to the appearance of an additional CO atop adsorption state having a characteristically higher vibrational frequency than that of the regular atop CO adsorbed on low-defect density terraces. These new defect states were both observed under UHV conditions with a CO exposure of

10 L (1 L = 10⁻⁶ Torr × s) as well as at elevated pressures (i.e. P_{CO} = 100 mbar). Upon dosing of the syngas (SG = CO + H₂) at 493 K, it was found that the atop CO adsorbed on the low-defect density terrace sites remained intact as spectator species, while the vibrational signal for the atop CO adsorbed on defect sites irreversibly attenuated, suggesting the active involvement of these sites in the polymerization and chain growth (FT) process. It was also shown that the hydrocarbon production was proportional to the surface defect density [77–79].

3.2.3.2 CO + H₂ Co-adsorption and Reaction on Pd(111) and Pd/Al₂O₃/NiAl(110) CO + H₂ co-adsorption and reaction at elevated pressures were also studied on clean and defect rich Pd(111) as well as Pd clusters deposited on alumina ultrathin films via SFG technique [42, 80, 81]. These studies revealed that clean Pd(111) single crystals surface was relatively unreactive for CO hydrogenation, mostly due to CO poisoning of the catalyst surface, while formation of CH_xO species (i.e. indication of CO hydrogenation) was observed on the defect-rich Pd(111) model catalyst surface [42]. In a similar fashion, generation of trace amounts of methane and methanol was also detected upon high-pressure CO + H₂ adsorption on the Pd/Al₂O₃/NiAl(110) model catalyst surface [81]. Indications for surface roughening on clean Pd(111) was also reported upon high pressure CO + H₂ adsorption [81].

3.2.4 CO + O₂ Co-adsorption and CO Oxidation Reaction

CO oxidation is a widely used test reaction for demonstrating the activity of heterogeneous catalytic prototypes. Thus, there exist a vast number of surface science studies elucidating the mechanism of this very important reaction over a large number of different model catalyst systems under various reaction conditions. Thus in this review, rather than providing a comprehensive “grand survey” of the mechanism of the CO + O₂ reaction on the previously investigated model catalyst surfaces under different reaction regimes, we will focus on various selected examples from the recent literature [64, 67–70, 82–97], demonstrating the power of the surface-sensitive in situ vibrational spectroscopic techniques at elevated pressures and highlight some of the very critical, yet controversial points which are subject of intense discussion in the current literature. For a detailed discussion on some of the general aspects of the heterogeneous catalytic CO oxidation reaction, the reader is referred to a recent review article and references therein [98].

Although seemingly a simple reaction, CO oxidation reaction on PGMs constitutes some of the most characteristic genres of mechanistic micro steps that are

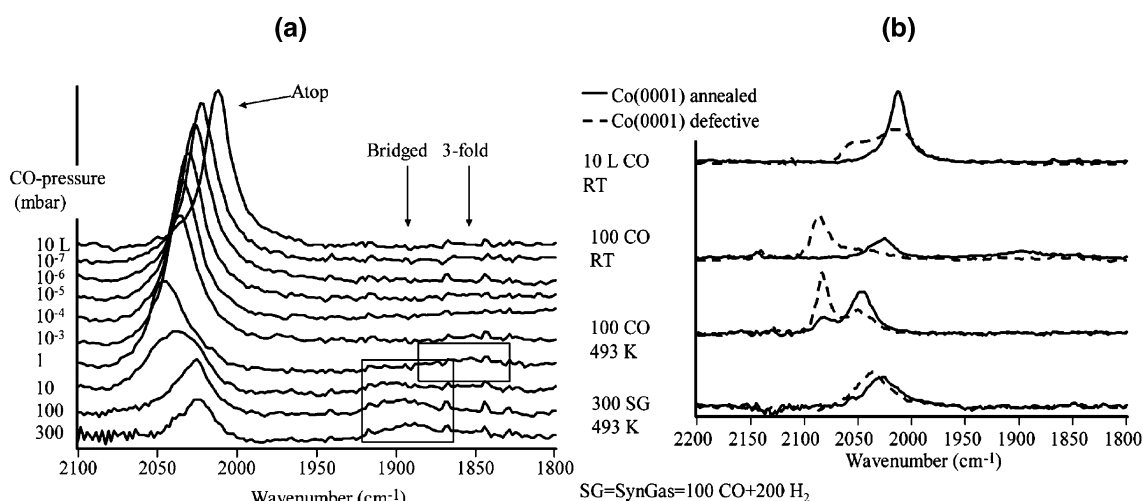


Fig. 17 **a** In-situ PM-IRAS data for CO adsorption on clean Co(0001) at room temperature (RT). **b** PM-IRAS data for CO and CO + H₂ (syngas) adsorption on low-defect density (annealed) and defective Co(0001) surfaces. CO adsorption is presented for UHV

conditions (10 L) at RT, 100 mbar at RT and 100 mbar at 493 K while 300 mbar of syngas (100 mbar CO + 200 mbar H₂) was dosed at 493 K

ubiquitous for many heterogeneous catalytic reactions, such as molecular adsorption and desorption of a reactant ($\text{CO(g)} \leftrightarrow \text{CO(ads)}$), dissociative adsorption of a reactant ($\text{O}_2(\text{g}) \leftrightarrow 2\text{O(ads)}$), reactive combination of adsorbates ($\text{CO(ads)} + \text{O(ads)} \rightarrow \text{CO}_2(\text{g})$), competition for adsorption sites leading to inhibition/poisoning, adsorbate induced surface morphology changes, surface/bulk oxide formation and oscillatory behavior (bistability) [64, 67–70, 82–98]. Goodman et al. provided some of the most recent and extensive studies on the CO + O₂ reaction on PGM single crystal model catalyst surfaces (e.g. Pt, Pd, Rh, Ru, AuPd) at elevated pressures via PM-IRAS technique [64, 67–70, 82–90] which will form the main focus of this review.

It is generally accepted that Langmuir–Hinshelwood reaction mechanism is valid for the CO oxidation on PGM single crystal surfaces at both low-pressure (i.e. UHV) as well as high-pressure (i.e. close to atmospheric pressure) conditions where the molecularly adsorbed CO reacts with the atomic oxygen on the surface (generated via dissociative adsorption of O₂(g)) forming CO₂ which quickly desorbs from the surface [64, 67–70, 82–98]. In other words, no “pressure-gap” effects were found on typical PGM single crystal model catalyst surfaces [88].

Under low pressure conditions, inhibition of O₂ adsorption due to a high CO(ads) coverage was found to be a much stronger factor than the alternative inhibition process associated with the inhibition of CO(ads) by atomic (surface) oxygen [88]. Thus the optimum reaction conditions under low pressures involve a low CO surface coverage. At low temperatures and pressures (i.e. under low reaction rate regime), reaction rate is limited by the CO

poisoning. Thus, increasing temperature under these conditions has a positive effect on the reaction rate until particularly high temperatures are reached, where the reaction rate starts to be limited by the surface oxygen inhibition decreasing the CO surface residence time and CO surface coverage. Such O-rich surfaces correspond to a high reaction rate regime [88]. Hence, most of the kinetic aspects of the CO oxidation reaction on PGM can be elucidated by considering the inhibition (competitive adsorption) pathways and the oscillatory oxidation/reduction of the catalyst surface. Therefore, ultimate reactivity could be obtained by optimizing the reaction conditions in order to control CO-inhibition/O-inhibition and oxidation of the PGM catalyst.

Under high pressure conditions, CO oxidation reaction on PGM single crystal model catalyst surfaces tend to have three typical kinetic regimes: (i) CO-inhibited low temperature regime with a low reaction rate, where the rate is controlled by CO desorption from the surface, (ii) a mass transfer limited (MTL) regime with a high reaction rate and (iii) a transient hyperactive (extremely fast) regime in between the first two regimes which is not controlled by MTL [82]. Under high pressures and low temperatures (CO-inhibited conditions), reaction rate exhibits first order dependence on O₂ partial pressures and a negative (~ -1) order dependence on CO partial pressures where the reaction rate is directly controlled by the rate of CO desorption from the surface. It has been reported that the apparent activation energies (E_a) of the CO oxidation reaction on Pt, Pd, Rh model catalysts were about 110 kJ/mol which is very close to the CO desorption energies of these surfaces. Thus under these conditions, reaction is clearly

structure insensitive. Ru exhibits an anomaly among other PGM, where although Ru is the least active surface at low pressures, it is found to be the most active surface at high pressures [83]. Higher activity of the Ru surface at elevated pressures and low temperatures was attributed to the higher tendency of this surface to be covered with oxygen atoms, reaching a CO-uninhibited regime more readily [83]. On Pd and Rh surfaces, under high pressures and high O₂ partial pressures, reaction was found to be inhibited by the deactivation due to oxidation of the metal catalysts forming oxide phases, however metallic Pt model catalysts were observed to be much more resistant towards surface oxidation, requiring extremely high oxygen partial pressures for deactivation (Fig. 18) [83]. Next few sections of this review, concentrate on the elevated-pressure CO oxidation reaction studies performed on a selected set of PGM single crystal model catalyst surfaces providing spectroscopic and kinetic evidences for the arguments discussed above.

3.2.4.1 CO Oxidation on Rh(111) Figure 19 presents a set of PM-IRAS results [82] obtained at different CO oxidation reaction conditions on Rh(111) whose overall kinetic behavior is described in Fig. 18a [88]. It is apparent that below 450 K (i.e. under low reaction rate conditions) CO is typically found to adsorb in both atop (with $\nu_{\text{CO}} < 2,100 \text{ cm}^{-1}$) and threefold configurations (with $1,850 \text{ cm}^{-1} < \nu_{\text{CO}} < 1,900 \text{ cm}^{-1}$), where threefold species disappear at high temperatures with increasing reaction rate (Fig. 18a). Probably one of the most important aspects of the vibrational features of adsorbed CO given in Fig. 19 is the fact that all of these frequencies match with

CO molecules adsorbed on a metallic Rh surface and not with RhO_x, as CO adsorption frequencies on oxidized Rh surfaces are expected to appear at much higher frequencies (e.g. $2,130 \text{ cm}^{-1}$). Interpretation of the spectroscopic data in Fig. 19 together with the kinetic results presented in Fig. 18a suggests that for low reaction rate (CO-inhibited) regime, CO exists predominantly in atop configuration whose vibrational frequency red shifts down to $\sim 2,065 \text{ cm}^{-1}$ with increasing temperatures/increasing reaction rates. Upon reaching the roll-over (i.e. steady state exhibiting a surface oxygen coverage higher than 0.5 ML), a new atop CO feature appears at $2,084 \text{ cm}^{-1}$. This latter feature was attributed to the CO adsorbed on an O-rich metallic Rh(111) surface which is comprised of chemisorbed atomic oxygen species on metallic Rh(111), rather than a surface or a bulk rhodium oxide.

Gao et al. [82] also demonstrated that under extremely O-rich conditions (i.e. O₂/CO = 8/1) at 460 K, metallic Rh(111) surface can be oxidized after a certain time period under the reaction conditions which is accompanied by a drastic fall in the reaction rate and concomitant appearance of a new CO adsorption feature at $2,130 \text{ cm}^{-1}$ associated with the atop CO adsorption on the oxide. Thus, these authors argued that neither bulk oxide nor surface oxides of Rh are active in CO oxidation reaction and the reaction is governed by simple Langmuir–Hinshelwood mechanism under steady state conditions where the active phase is comprised of O-rich ($\theta_{\text{CO}} > 0.5 \text{ ML}$) metallic Rh(111) surface. Although interpretation of the experimental results of Goodman et al. summarized above seems to be self-consistent, these results were recently challenged by high-pressure surface X-ray diffraction (SXRD) results by

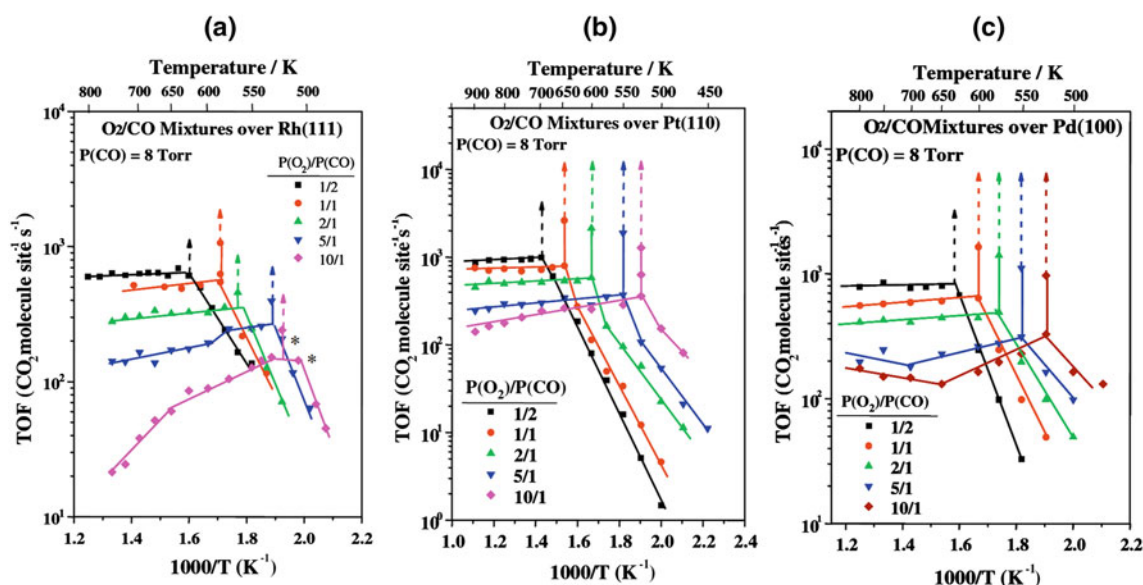
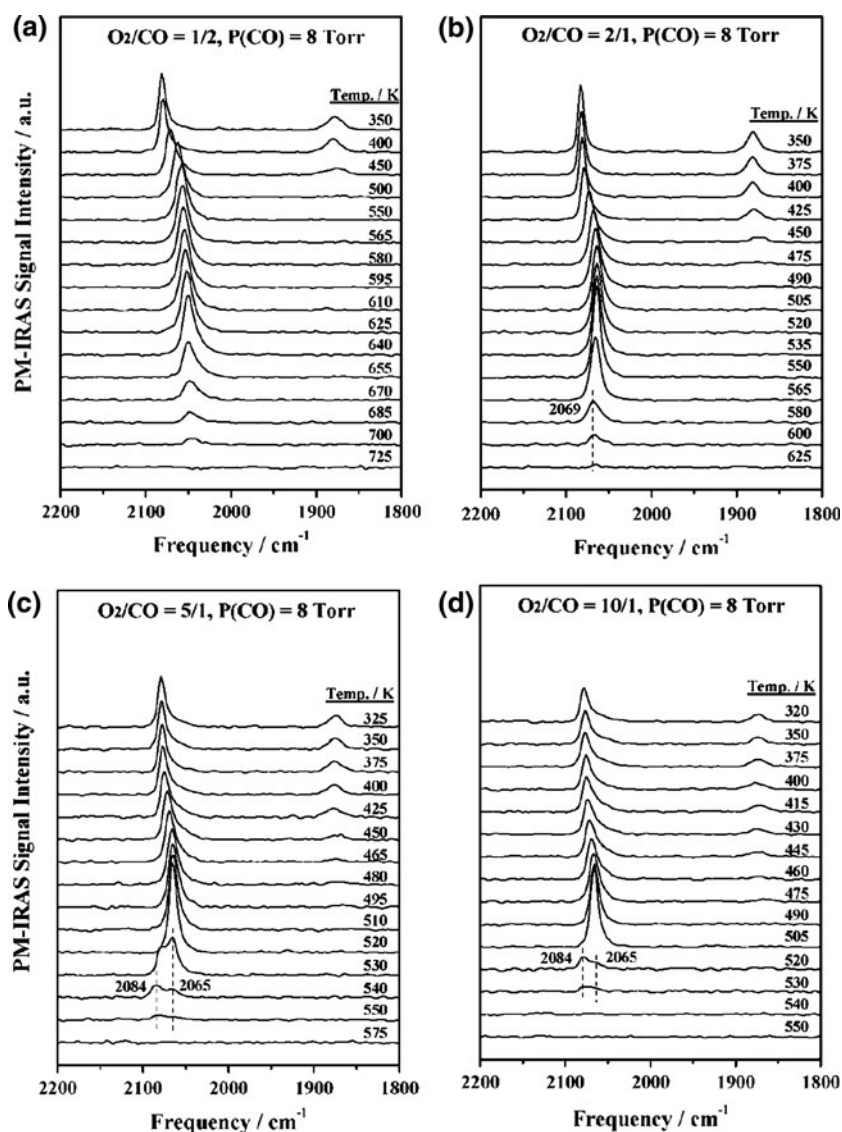


Fig. 18 CO₂ turn over frequency (TOF) values for CO + O₂ reaction on **a** Rh(111), **b** Pt(110) and **c** Pd(100) at various temperatures and reactant compositions where partial pressure of CO is kept constant at 8 Torr [83, 88]

Fig. 19 CO + O₂ reaction on Rh(111) at various temperatures via PM-IRAS as a function of reactant compositions where partial pressure of CO is kept constant at 8 Torr. **a** O₂/CO = 1/2 mixture (stoichiometric), **b** O₂/CO = 2/1 mixture (mildly excess in O₂), **c** O₂/CO = 5/1 mixture (moderately excess in O₂) and **d** O₂/CO = 10/1 mixture (heavily excess in O₂) [82]



Gustafson et al. [91, 92] who argued that contribution from a “surface oxide” phase of rhodium to the high reaction rate should not be excluded.

3.2.4.2 CO Oxidation on Pd(100) Similar PM-IRAS (Fig. 20) and kinetic studies (Figs. 18c, 20b) on the CO oxidation reaction was also extended to Pd(100) model catalyst surfaces by Goodman and co-workers [87]. These authors reported that under the steady state reaction conditions at low pressures, CO oxidation reaction was found to be only CO-inhibited without any sign of O-inhibition. Furthermore, under these conditions, CO conversion was found to be “collision-limited” and the optimized CO conversion is independent of the O₂/CO for $P_{\text{CO}} \leq 1 \times 10^{-4}$ Torr, where the CO surface coverage was always extremely low [87]. On the other hand, under high pressures, three different reaction regimes were observed as in the case of Rh(111) [87]: (i) CO-inhibited low

temperature regime with a low reaction rate, (ii) a MTL regime after the “roll-over” with a high reaction rate and (iii) a transient hyperactive (extremely fast) regime in between. PM-IRAS data given in Fig. 20a–d suggest that under the CO-inhibited regime CO exhibits vibrational frequencies above $1,960 \text{ cm}^{-1}$ corresponding to bridging CO with a surface coverage greater than 0.6 ML. For the stoichiometric (Fig. 20a) and mildly oxidizing (Fig. 20b) reactant mixtures, no CO species other than bridging CO was detected. Just after the roll-over, a steady state high reactivity regime is reached with θ_{CO} close to zero. On the other hand a quite interesting behavior is observed for moderately/strongly O₂-rich gas mixtures (Fig. 20c–e). For these O₂-rich gas mixtures, in the CO-inhibited regime (i.e. within 300–525 K), reaction rate increases with increasing temperature as a function of decreasing θ_{CO} (Fig. 18c, e, region (i)). At 500–525 K the transient hyperactive state is reached (Fig. 18c, 20e, region (ii)) which has almost no

adsorbed CO on the surface. However a further increase in temperature to 550 K results in a sharp fall in reaction rate (Fig. 18c, 20e, region (iii)) and the concomitant formation of two new features in PM-IRAS data at 2,087 and 2,142 cm^{-1} which were assigned to the CO adsorbed on 3D surface oxide (but not bulk PdO) formed on the Pd(100) model catalyst surface. This 3D surface oxide phase was argued to be a less reactive phase resulting in a decrease in the reaction rate below the MTL reaction rate (Fig. 18c). Increasing the temperature above 550 K leads to the disappearance of the 2,087 and 2,142 cm^{-1} features which is accompanied by an increase in the reaction rate back to MTL value, indicating the thermal decomposition of the inactive PdO_x surface oxide. Such arguments were also supported by other studies performed on high surface area (powder) Pd/ Al_2O_3 surfaces [99] favoring the active phase being the “O-covered metal surface” rather than the surface oxide. It is worth mentioning that Frenken and co-workers [93, 100] disagreed with these interpretations and claimed via XRD experiments that the active phase in CO oxidation on Pd(100) is a surface oxide phase rather than the O-chemisorbed metallic Pd(100) surface.

3.2.4.3 CO Oxidation on Pt(110) Analogous elevated-pressure CO oxidation reaction studies on Pt(110) by Goodman and co-workers [87] suggested that Pt(110) surface has similar CO-inhibited and hyperactive regimes which is followed by a roll-over leading to a high reaction-rate (steady state) regime at elevated temperatures. Probably the most striking difference of the Pt(110) surface compared to Pd(100) and Rh(111) is the fact that even under extremely O_2 -rich gas mixtures (i.e. $\text{O}_2/\text{CO} = 1/10$) no indications of Pt oxidation was observed via PM-IRAS. In other words, for all of the investigated gas compositions and temperatures, CO vibrational signal in PM-IRAS was found to be within 2,050–2,110 cm^{-1} and no CO vibrational signal above 2,110 cm^{-1} (a characteristic signature of oxide surfaces) was detected revealing the strong oxidation resistance of Pt(110) surface with respect to that of Pd(100) and Rh(111).

3.2.4.4 CO Oxidation on Ru(0001) and RuO₂ As mentioned in earlier sections, Ru surfaces present an anomalous case in the CO oxidation reaction. In order to address this issue, Goodman and co-workers [83, 90] investigated the

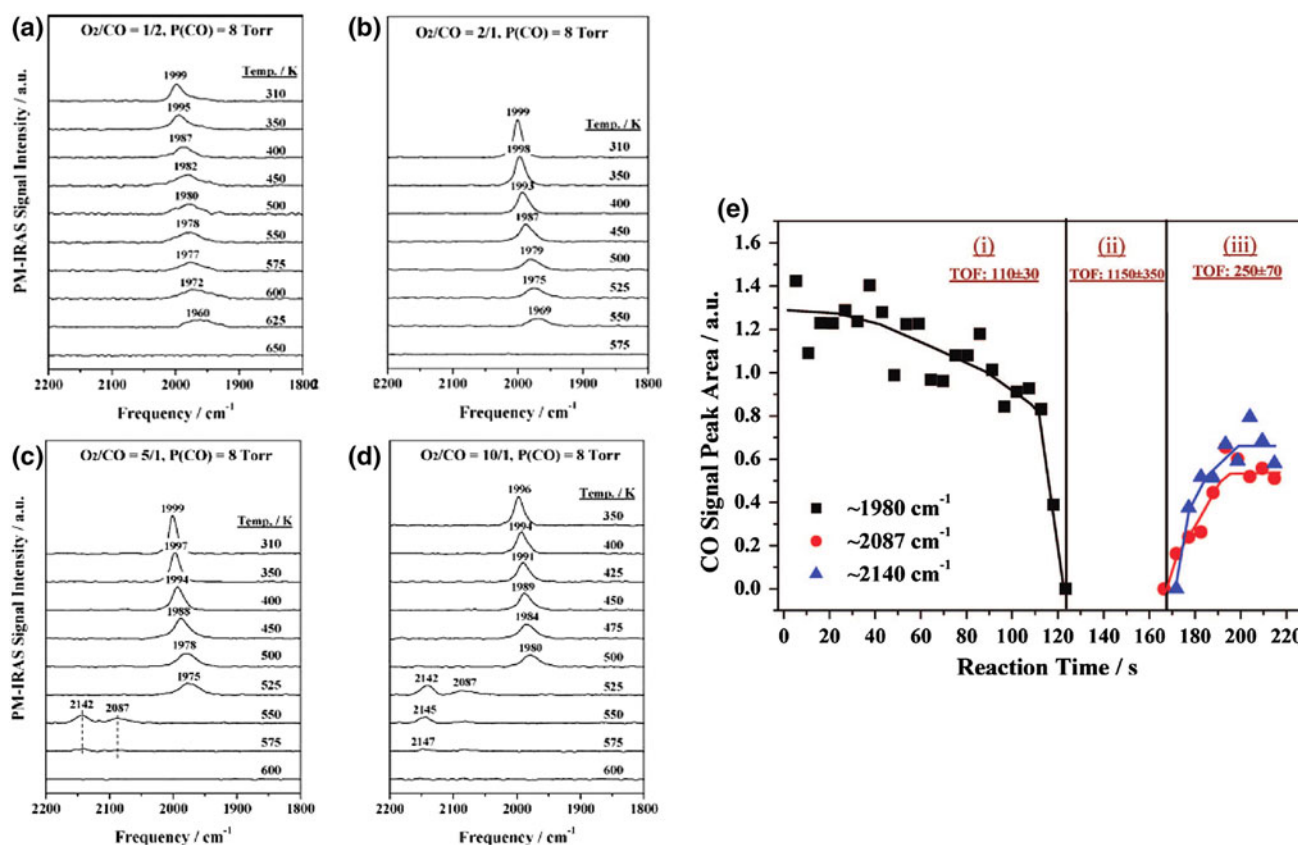


Fig. 20 CO + O_2 reaction on Pd(100) at various temperatures via PM-IRAS as a function of reactant compositions where partial pressure of CO is kept constant at 8 Torr. **a** $\text{O}_2/\text{CO} = 1/2$ mixture (stoichiometric), **b** $\text{O}_2/\text{CO} = 2/1$ mixture (mildly excess in O_2),

c $\text{O}_2/\text{CO} = 5/1$ mixture (moderately excess in O_2), **d** $\text{O}_2/\text{CO} = 10/1$ mixture (heavily excess in O_2), **e** integrated CO signals at 1980, 2087 and 2140 cm^{-1} in PM-IRAS as a function of time for a $\text{O}_2/\text{CO} = 10/1$ mixture with $P_{\text{CO}} = 2$ Torr at 500 K [87]

behavior of the metallic (Ru(0001) and oxide (RuO₂(110)/Ru(0001)) model catalyst surfaces using kinetic and spectroscopic techniques. These studies revealed that on Ru(0001), under stoichiometric and reducing conditions within 300–700 K as well as under net-oxidizing conditions below 475 K, the most active phase was determined to be a metallic Ru(0001) surface which was covered with chemisorbed oxygen. This chemisorbed oxygen was also found to be thermodynamically stable phase, which can readily exist under these reaction conditions, where the CO oxidation reaction was reported to occur predominantly on the surface defect sites of the (1 × 1)-O/Ru(0001). The density of these sites was reported to be between 0.01–1 × 10⁻⁵ ML, while the CO adsorption energy on these sites (i.e. 68 kJ/mol) is significantly lower than that of the O-covered Pd, Pt and Rh (i.e. ~ 100 kJ/mol) and RuO₂ (i.e. ~ 120 kJ/mol) [83, 90]. On the other hand, RuO₂(110)/Ru(0001) model catalyst prepared by growing an oxide ultrathin film on the metallic Ru(0001) substrate, was active and stable only at temperatures above 475 K and under net-oxidizing conditions. Furthermore, it was also pointed out that pure RuO₂ in the absence of a metal substrate and strong metal support interaction or “SMSI” was not active. It was also demonstrated that for a stoichiometric gas mixture, the oxide ultrathin film on the RuO₂(110)/Ru(0001) model catalyst surface was readily reduced to the metallic O-covered state (active phase).

On the other hand, under net-oxidizing conditions (i.e. O₂/CO = 5/1) and at 550 K, (1 × 1)-O/Ru(0001) surface was observed to transform into RuO₂(110)/Ru(0001) where the oxide phase revealed 4 times higher conversion than the (1 × 1)-O/Ru(0001) surface [83, 90]. However, Goodman and co-workers [83] emphasized that this observation should not be interpreted in a universal fashion in order to assign a higher activity for RuO₂ than a metallic Ru surface; as RuO₂ phase is not stable below 500 K under reaction conditions. Furthermore, when the activity of these two surfaces were compared in a “per-active site” basis, (1 × 1)-O/Ru(0001) surface where active sites were reported to be the defect sites with a surface coverage as low as 10⁻⁵ ML seems to be more active than the RuO₂(110)/Ru(0001) surface having active coordinatively unsaturated cus-Ru sites with a coverage of 10⁻¹ ML [83]. PM-IRAS experiments performed by these authors during the CO + O₂ reaction on RuO₂(110)/Ru(0001) surface revealed that assignment of CO vibrational features were rather complex. It was reported that on this surface: (i), $\nu_{\text{CO}} \sim 2,050 \text{ cm}^{-1}$ was assigned to CO on reduced metallic Ru; (ii) $2,050 \text{ cm}^{-1} < \nu_{\text{CO}} < 2,080 \text{ cm}^{-1}$ was attributed to oxygen-covered metallic Ru with $\theta_{\text{o(ads)}} \leq 0.5 \text{ ML}$; (iii) $\nu_{\text{CO}} > 2,080 \text{ cm}^{-1}$ was associated with CO on metallic Ru having a high $\theta_{\text{o(ads)}}$ or RuO₂ or RuO_x; while (iv) $\nu_{\text{CO}} \sim 2,130\text{--}2,140/2,060\text{--}2,080 \text{ cm}^{-1}$ bands could also be

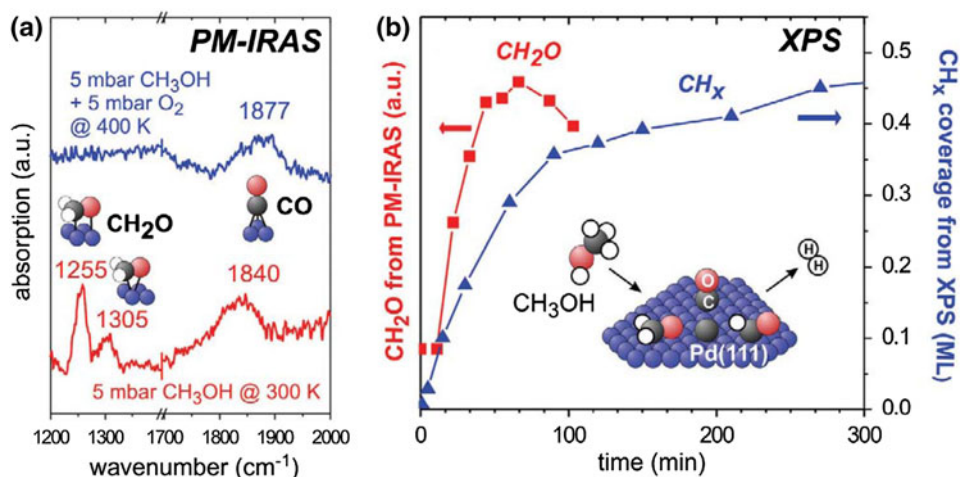
assigned to ruthenium carbonyl species (i.e. Ru^{x+}(CO)_y) [83].

3.2.4.5 CO Oxidation on Au–Pd Bimetallic Alloy Catalysts In a recent set of interesting reports, Goodman and co-workers [67, 68] investigated the elevated pressure CO + O₂ reaction via PM-IRAS on Au–Pd bimetallic alloy catalysts in various forms such as bimetallic single crystals (AuPd(100)), bimetallic Au–Pd alloy thin films grown on Mo(110) [70] and bimetallic Au–Pd alloy nanoparticles deposited on TiO₂ ultrathin films grown on Mo(110) [70]. It was reported that at low pressures, alloying with Au leads to alterations in the electronic structure and the reaction activation energy as well as the formation of isolated Pd sites which are incapable of O₂ dissociation revealing a relatively less active surface. However at elevated pressures, upon surface segregation of Pd and the formation of contiguous Pd sites, a high activity was observed (even at low temperatures). As a result of the lower CO adsorption strength on the Au–Pd alloys, these systems show superior CO oxidation performance compared to pure Pd catalysts which exhibit severe CO-inhibition for stoichiometric mixtures at elevated pressures and low temperatures. On the other hand, under net-oxidizing conditions at elevated pressures, Pd reveals a higher initial activity than Au–Pd bimetallic systems due to its higher O₂ activation/dissociation capability. Owing to the low oxidation resistance of Pd catalysts, these surfaces quickly lose their CO oxidation activity under net oxidizing conditions while the Au–Pd alloy systems can robustly sustain their metallic structure and catalytic performance under the same conditions [70]. Furthermore, bimetallic single crystals, bimetallic Au–Pd alloy thin films grown on Mo(110) and bimetallic Au–Pd alloy nanoparticles deposited on TiO₂ ultrathin films grown on Mo(110) showed similar kinetic behavior highlighting the structure insensitivity of this reaction at elevated pressures [70]. These interesting studies suggest that Au–Pd systems can be potentially used as highly active and extremely stable oxidation catalysts in many industrial applications.

3.2.5 Methanol Adsorption and Reaction on Pd-Based Model Catalysts

Methanol adsorption, decomposition/partial oxidation and methanol steam reforming (MSR) reactions have been extensively studied via SFG and PM-IRAS on different forms of Pd-containing model catalyst surfaces in the literature. For a detailed discussion of these model catalyst studies and other mechanistic aspects of these reactions, reader is referred to a recent review article by Bäumer et al. and references therein [101]. Some of the earlier and informative surface science studies on methanol adsorption

Fig. 21 **a** PM-IRAS data for methanol decomposition (*bottom* spectrum) and methanol oxidation (*top* spectrum) on Pd(111) at elevated pressures. **b** Time dependent evolution of CH₂O and CH_x species during the methanol decomposition reaction [104]



and reactions on single crystal surfaces can also be found in References [102, 103]. Figure 21a presents elevated pressure methanol decomposition and methanol partial oxidation experiments performed on Pd(111) via PM-IRAS technique [104, 105]. Bottom spectrum in Fig. 21a corresponds to methanol decomposition at 300 K with $P_{\text{MeOH}} = 5$ mbar, revealing the formation of surface CH₂O and CO species. Complementary XPS studies (Fig. 21b) performed along with the PM-IRAS experiments indicated a direct correlation between CH₂O formation and accumulation of carbonaceous (CH_x) species on the surface. Top spectrum in Fig. 21a is associated with methanol oxidation in the presence of oxygen where it was found that the CO₂ yield is enhanced on the C-modified Pd(111) surface, compared to a clean Pd(111) surface.

In a more recent study, Rameshan et al. [106] examined MSR reaction ($\text{CH}_3\text{OH} + \text{H}_2\text{O} \rightarrow \text{CO}_2 + 3\text{H}_2$) on PdZn(1:1)/Pd(111) bimetallic catalyst surface at elevated pressures via PM-IRAS. These studies showed that CO₂ selectivity of the PdZn 1:1 bimetallic surface alloy in MSR reaction was dictated by the subsurface layer structure. Along these lines, while a five-layer PdZn 1:1 multilayer system revealed a high selectivity towards CO₂; PdZn 1:1 monolayer surface produced exclusively CO and H₂ rather than CO₂. Furthermore using CO adsorption via PM-IRAS, variations in the surface composition of the bimetallic system at elevated temperatures and pressures were also monitored (Fig. 22). Top spectrum in Fig. 22 corresponds to CO adsorption on a multilayer PdZn (1:1) alloy annealed at 573 K, exhibiting a homogenous surface composition, where CO adsorbs only in atop configuration (2,071 cm⁻¹) due to the lack of contiguous Pd sites. Upon annealing the multilayer PdZn (1:1) alloy at 623 K, complementary LEIS experiments suggested that the surface became richer in Pd. This is also evident in the corresponding PM-IRAS spectrum in Fig. 22 (middle spectrum) presenting the existence

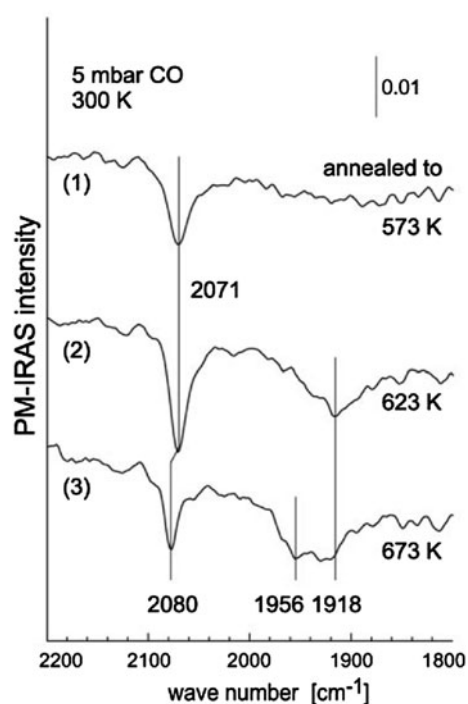


Fig. 22 PM-IRAS data for 5 mbar CO adsorption at 300 K on a multilayer PdZn (1:1) alloy which is previously annealed at 573, 623 and 673 K [106]

of a new feature at 1,918 cm⁻¹. Annealing at higher temperatures such as 673 K led to a further enrichment of the surface with Pd and the generation of a 1,956 cm⁻¹ CO vibrational signal associated with bridging CO on contiguous surface Pd sites [106].

4 Conclusions and Outlook

Monitoring the surface chemistry of heterogeneous catalysts under industrially relevant conditions such as elevated

temperatures and pressures is a challenging yet an extremely rewarding task which requires dedicated in situ spectroscopy methods. Due to their photons-in, photons-out nature, vibrational spectroscopic techniques offer a very powerful and a versatile experimental tool box, allowing real-time investigation of working catalyst surfaces at elevated pressures. IRAS, polarization modulation-IRAS (PM-IRAS or PM-IRRAS), SFG techniques reveal valuable surface chemical information at the molecular level, particularly when they are applied to atomically well-defined planar model catalyst surfaces such as single crystals or ultrathin films. In this review article, recent state of the art applications of in situ surface vibrational spectroscopy were presented with a particular focus on elevated pressure adsorption of probe molecules (e.g. CO, NO, O₂, H₂, CH₃OH,) on monometallic and bimetallic transition metal surfaces (e.g. Pt, Pd, Rh, Au, Co, PdZn, AuPd, CuPt). Furthermore, elevated pressure carbon monoxide oxidation, and CO hydrogenation, Fischer–Tropsch, methanol decomposition/partial oxidation and MSR reactions on single crystal PGM surfaces were discussed. Different case studies were discussed in order to demonstrate the capabilities, opportunities and the existing challenges associated with the in situ vibrational spectroscopic analysis of heterogeneous catalytic reactions on model catalyst surfaces at elevated pressures. These examples clearly indicate that although certain catalytic systems (e.g. CO/Pd(111)) lack a “pressure gap” where UHV experiments provide an excellent description of the catalytic system at elevated pressures, other simple model catalyst systems such as NO/Pd(111) reveals a “pressure gap”, where observation of various novel catalytic species becomes only possible under elevated temperatures and pressures. These case studies point to the fact that rather than relying solely on conventional UHV surface science experiments on model catalyst systems, in situ surface sensitive vibrational spectroscopic techniques such as PM-IRAS and SFG should be complemented with the conventional UHV methods in order to obtain a realistic and an accurate view of the working catalysts at the molecular level.

Acknowledgments E.O. acknowledges support from Turkish Academy of Sciences (TUBA) through the “Outstanding Young Investigator” Grant. E.V. acknowledges RFBR (Russia) #12-03-91373-CT_a for financial support.

References

- Niemantsverdriet JW (2007) Spectroscopy in catalysis. VCH Verlagsgesellschaft mbH, Weinheim
- Ruppender HJ, Grunze M, Kong CW, Wilmers M (1990) Surf Interface Anal 15:245–253
- Ogletree DF, Bluhm H, Lebedev G, Fadley CS, Hussain Z, Salmeron M (2002) Rev Sci Instrum 73:3872–3877
- Pantforder J, Pollmann S, Zhu JF, Borgmann D, Denecke R, Steinruck HP (2005) Rev Sci Instrum 76:014102/1-014102/9
- Laegsgaard E, Osterlund L, Thostrup P, Rasmussen PB, Stensgaard I, Besenbacher F (2001) Rev Sci Instrum 72:3537–3542
- Jensen JA, Rider KB, Chen Y, Salmeron M, Somorjai GA (1999) J Vac Sci Technol B 17:1080–1084
- McIntyre BJ, Salmeron M, Somorjai GA (1993) Rev Sci Instrum 64:687–691
- Rasmussen PB, Hendriksen BLM, Zeijlemaker H, Ficke HG, Frenken JWM (1998) Rev Sci Instrum 69:3879–3884
- Gao F, Goodman DW (2012) Annu Rev Phys Chem 63:265–286
- Hoffmann FM (1983) Surf Sci Rep 3:109–192
- Chabal YJ (1988) Surf Sci Rep 8:211–357
- Kunimatsu K, Golden WG, Seki H, Philpott MR (1985) Langmuir 1:245–250
- Green MJ, Barner BJ, Corn RM (1991) Rev Sci Instrum 62:1426–1430
- Barner BJ, Green MJ, Saez EI, Corn RM (1991) Anal Chem 63:55–60
- Blaudez D, Buffeteau T, Cornut JC, Desbat B, Escafre N, Pezolet M, Turlet JM (1993) Appl Spectrosc 47:869–874
- Faguy PW, Richmond WN, Jackson RS, Weibel SC, Ball G, Payer JH (1998) Appl Spectrosc 52:557–564
- Ozensoy E (2004) Ph.D. Thesis. Texas A&M University
- Ozensoy E, Hess C, Goodman DW (2004) Top Catal 28:13–23
- Ozensoy E, Meier DC, Goodman DW (2002) J Phys Chem B 106:9367–9371
- Ozensoy E, Min BK, Goodman DW (2004) J Phys Chem B 108:4351–4357
- Ozensoy E, Goodman DW (2004) Phys Chem Chem Phys 6:3765–3778 and references therein
- Ozensoy E, Hess C, Loffreda D, Sautet S, Goodman DW (2005) J Phys Chem B 109:5414–5417
- Hess C, Ozensoy E, Yi CW, Goodman DW (2006) J Am Chem Soc 128:2988–2994
- Ozensoy E, Hess C, Goodman DW (2002) J Am Chem Soc 124:8524–8525 and references therein
- Hess C, Ozensoy E, Goodman DW (2003) J Phys Chem B 107:2759–2764
- Hess C, Ozensoy E, Goodman DW (2004) J Phys Chem B 108:14181–14182
- Shen YR (1994) Surf Sci 299–300:551–562
- Shen YR (1989) Nature 337:519–525
- Rupprechter G (2007) Adv Catal 51:133–263
- Vidal F, Tadjeddine A (2005) Rep Prog Phys 68:1095–1127
- Lambert AG, Davies PB, Neivandt DJ (2005) Appl Spectrosc Rev 40:103–145
- Moad AJ, Simpson GJ (2004) J Phys Chem B 108:3548–3562
- Cremer PS, Somorjai GA (1995) J Chem Soc Faraday Trans 91:3671–3677
- Cremer PS, Su XC, Shen YR, Somorjai GA (1996) J Am Chem Soc 118:2942–2949
- Rupprechter G (2007) MRS Bull 32:1031–1037
- Kuhn WK, Szanyi J, Goodman DW (1992) Surf Sci 274:L611–L618
- Stacchiola D, Thompson AW, Kaltchev M, Tysoe WT (2002) J Vac Sci Technol B 20:2101–2105
- Rose MK, Mitsui T, Dunphy J, Borg A, Ogletree DF, Salmeron M, Sautet P (2002) Surf Sci 512:48–60
- Unterhalt H, Rupprechter G, Freund HJ (2002) J Phys Chem B 106:356–367
- Rupprechter G, Unterhalt H, Morkel M, Galletto P, Hu LJ, Freund HJ (2002) Surf Sci 502:109–122
- Kaichev VV, Prosvirin IP, Bukhtiyarov VI, Unterhalt H, Rupprechter G, Freund HJ (2003) J Phys Chem B 107:3522–3527

42. Rupprechter G, Kaichev VV, Unterhalt H, Morkel A, Bukhtiyarov VI (2004) *Appl Surf Sci* 235:26–31
43. Szanyi J, Kuhn WK, Goodman DW (1993) *J Vac Sci Technol A* 11:1969–1974
44. Goodman DW (1994) *Surf Sci* 299:837–848
45. Baumer M, Freund HJ (1999) *Prog Surf Sci* 61:127–198
46. Bowker M, Holroyd R, Perkins N, Bhanoo J, Counsell J, Carley A, Morgan C (2007) *Surf Sci* 601:3651–3660
47. Föttinger K, Schlögl R, Rupprechter G (2008) *Chem Commun* 0:320–322
48. Rupprechter G (2001) *Phys Chem Chem Phys* 3:4621–4632
49. Yudanov IV, Sahnoun R, Neyman KM, Rosch N, Hoffmann J, Schauermann S, Johaneck V, Unterhalt H, Rupprechter G, Libuda J, Freund HJ (2003) *J Phys Chem B* 107:255–264
50. Dellwig T, Rupprechter G, Unterhalt H, Freund H-J (2000) *Phys Rev Lett* 85:776–779
51. Ertl G, Neumann M, Streit KM (1977) *Surf Sci* 64:393–410
52. Pedersen MO, Bocquet ML, Sautet P, Lægsgaard E, Stensgaard I, Besenbacher F (1999) *Chem Phys Lett* 299:403–409
53. Carrasco E, Aumer A, Brown MA, Dowler R, Palacio I, Song S, Sterrer M (2010) *Surf Sci* 604:1320–1325
54. Su X, Cremer PS, Shen YR, Somorjai GA (1996) *Phys Rev Lett* 77:3858–3860
55. Avery NR (1981) *J Chem Phys* 74:4202–4203
56. Andersson KJ, Chorkendorff I (2010) *Surf Sci* 604:1733–1736
57. Haruta M, Yamada N, Kobayashi T, Iijima S (1989) *J Catal* 115:301–309
58. Haruta M (2002) *Cattech* 6:102–115
59. Valden M, Lai X, Goodman DW (1998) *Science* 281:1647–1650
60. Gong J (2012) *Chem Rev* 112: 2987–3054 and references therein
61. Piccolo L, Loffreda D, Cadete Santos Aires FJ, Deranlot C, Jugnet Y, Sautet P, Bertolini JC (2004) *Surf Sci* 566–568:995–1000
62. Nakamura I, Takahashi A, Fujitani T (2009) *Catal Lett* 129:400–403
63. Artiglia L, Diemant T, Hartmann H, Bansmann J, Behm RJ, Gavioli G, Cavaliere E, Granozzi G (2010) *Phys Chem Chem Phys* 12:6864–6874
64. Gao F, Wood TE, Goodman DW (2010) *Catal Lett* 134:9–12
65. Paszti Z, Hakkal O, Keszthelyi T, Berko A, Balazs N, Bako I, Guzzi L (2010) *Langmuir* 26:16312–16324
66. Diemant T, Hartmann H, Bansmann J, Behm RJ (2007) *J Catal* 252:171–177
67. Gao F, Wang Y, Goodman DW (2009) *J Am Chem Soc* 131:5734–5735
68. Gao F, Wang Y, Goodman DW (2009) *J Phys Chem C* 113:14993–15000
69. Gao F, Wang Y, Goodman DW (2009) *J Catal* 268:115–121 and references therein
70. Gao F, Wang Y, Goodman DW (2010) *J Phys Chem C* 114:4036–4043
71. Jugnet Y, Aires FJCS, Deranlot C, Piccolo L, Bertolini JC (2002) *Surf Sci* 521:L639–L644
72. Chen PJ, Goodman DW (1993) *Surf Sci* 297:L93–L99
73. Wallace WT, Cai Y, Chen MS, Goodman DW (2006) *J Phys Chem B* 110:6245–6249
74. Jones JE, Trenary M (2008) *J Phys Chem C* 112:20443–20450
75. Németh R, Kiss J, Solymosi F (2007) *J Phys Chem C* 111:1424–1427
76. Solymosi F, Bansagi T, Zakar TS (2004) *J Phys Chem B* 108:14178–14180
77. Oosterbeek H (2007) *Phys Chem Chem Phys* 9:3570–3576
78. Beitel GA, de Groot CPM, Oosterbeek H, Wilson JH (1997) *J Phys Chem B* 101:4035–4043
79. Beitel GA, Laskov A, Oosterbeek H, Kuipers EW (1996) *J Phys Chem* 100:12494–12502
80. Morkel M, Rupprechter G, Hans-Joachim Freund HJ (2005) *Surf Sci* 588:L209–L219
81. Morkel M, Rupprechter G, Hans-Joachim Freund HJ (2003) *J Chem Phys* 119:10853–10866
82. Gao F, Cai Y, Gath K, Wang Y, Chen MS, Guo QL, Goodman DW (2009) *J Phys Chem C* 113:182–192
83. Gao F, Goodman DW (2012) *Phys Chem Chem Phys* 14:6688–6697 and references therein
84. Gao F, McClure S, Chen M, Goodman DW (2010) *J Phys Chem C* 114:22369–22371
85. Gao F, Goodman DW (2010) *Langmuir* 26:16540–16551
86. McClure SM, Lundwall M, Yang F, Zhou Z, Goodman DW (2009) *J Phys Chem C* 113:9688–9697
87. Gao F, Wang Y, Cai Y, Goodman DW (2009) *J Phys Chem C* 113:174–181
88. McClure SM, Goodman DW (2009) *Chem Phys Lett* 469:1–13 and references therein
89. Gao F, McClure SM, Cai Y, Gath KK, Wang Y, Chen MS, Guo QL, Goodman DW (2009) *Surf Sci* 603:65–70
90. Gao F, Wang Y, Cai Y, Goodman DW (2009) *Surf Sci* 603:1126–1134
91. Gustafson J, Westerstrom R, Balmes O, Resta A, van Rijn R, Torrelles X, Herbschleb CT, Frenken JWM, Lundgren E (2010) *J Phys Chem C* 114:4580–4583
92. Gustafson J, Westerstrom R, Balmes O, Resta A, van Rijn R, Torrelles X, Herbschleb CT, Frenken JWM, Lundgren E (2010) *J Phys Chem C* 114:22372–22373
93. Rijn R, Balmes O, Felici R, Gustafson J, Wermeille D, Westerstrom R, Lundgren E, Frenken JWM (2010) *J Phys Chem C* 114:6875–6876
94. Dupont C, Loffreda D, Delbecq F, Aires FJCS, Ehret E, Jugnet Y (2008) *J Phys Chem C* 112:10862–19867
95. Dupont C, Delbecq F, Loffreda D, Jugnet Y (2011) *J Catal* 278:239–245
96. Sales BC, Turner JE, Maple MB (1982) *Surf Sci* 114:381–394
97. Ladas S, Imbihl R, Ertl G (1989) *Surf Sci* 219:88–106
98. Freund HJ, Meijer G, Scheffler M, Schlögl R, Wolf M (2011) *Angew Chem Int Ed* 50:10064–10094
99. Zorn K, Giorgio S, Halwax E, Henry CR, Gronbeck H, Rupprechter G (2011) *J Phys Chem C* 115:1103–1111
100. Gao F, Wang Y, Goodman DW (2010) *J Phys Chem C* 114:6874
101. Baumer M, Libuda J, Neyman KM, Rosch N, Rupprechter G, Freund HJ (2007) *Phys Chem Chem Phys* 9:3541–3558
102. Levis RJ, Jiang ZC, Winograd N (1989) *J Am Chem Soc* 111:4605–4612
103. Guo X, Hanley L, Yates JT (1989) *J Am Chem Soc* 111:3155–3157
104. Rupprechter G, Weilach C (2007) *Nano Today* 2:20–29
105. Borasio M, Fuente OR, Rupprechter G, Freund HJ (2005) *J Phys Chem B* 109:17791–17794
106. Rameshan C, Stadlmayr W, Weilach C, Penner S, Lorenz H, Havecker M, Blume R, Rocha T, Teschner D, Knop-Gericke A, Schlögl R, Memmel N, Zemlyanov D, Rupprechter G, Klotzer B (2010) *Angew Chem Int Ed* 49:3224–3227 and references therein